Summer 7-10-2019

Early Mississippian ocean anoxia triggering organic carbon burial and enhancing Late Paleozoic Ice Age onset: evidence from uranium isotopes of marine limestones

Keyi Cheng
Earth and Planetary Sciences

Keyi Cheng
Candidate

Earth and Planetary Sciences
Department

This thesis is approved, and it is acceptable in quality and form for publication:

Approved by the Thesis Committee:

Dr. Maya Elrick, Earth and Planetary Sciences, Chairperson

Dr. Stephen Romaniello, Arizona State University

Dr. Peter Fawcett, Earth and Planetary Sciences

EARLY MISSISSIPPIAN OCEAN ANOXIA TRIGGERING ORGANIC CARBON BURIAL AND ENHANCING LATE PALEOZOIC ICE AGE ONSET: EVIDENCE FROM URANIUM ISOTOPES OF MARINE LIMESTONES

by

KEYI CHENG

BACHELOR OF SCIENCE, GEOCHEMISTRY
CHINA UNIVERSITY OF GEOSCIENCES (WUHAN), 2016

THESIS

Submitted in Partial Fulfillment of the
Requirements for the Degree of

Master of Science
Earth and Planetary Sciences

The University of New Mexico
Albuquerque, New Mexico

July, 2019

ACKNOWLEDGMENTS

I sincerely acknowledge my advisor and dissertation chair, Dr. Maya Elrick, for her guidance, encouragement and patience during my two-year study at UNM. She sets up an example of a great advisor and a knowledgeable geologist from whom I would learn during my future career.

I also thank my committee members, Dr. Stephen Romaniello and Dr. Peter Fawcett, for their assistance in sample analysis and valuable suggestion about my research. This research could not be done without Steve's assistance in lab work at ASU and suggestions on quantitative methods, and Peter's ideas about paleoclimatology. Also a big thank to Dr. Geoff Gilleaudeau, for his assistance in field work.

I acknowledge NSF grant No. 1733598 (Elrick) for providing fund for this research.

Also I would like to thank my friends at EPS, I am always cheerful, relaxed and motivated staying with them. Thank you bro, Zhiyuan Ren, for bringing me so much happiness as my officemate. Special thank to Han Zhang and his cat, Xiao Ka (Cavendish). Thank you my parents for your encouragement and support during these years, I love you. To my ex-girlfriend Yuwei An, thank you for staying with me during those years. I greatly appreciate your support and encouragement.

EARLY MISSISSIPPIAN OCEAN ANOXIA TRIGGERING ORGANIC CARBON BURIAL AND ENHANCING LATE PALEOZOIC ICE AGE ONSET: EVIDENCE FROM URANIUM ISOTOPES OF MARINE LIMESTONES

By

Keyi Cheng

B.S., Geochemistry, China University of Geosciences (Wuhan), 2016

M.S., Earth and Planetary Science, University of New Mexico, 2019

ABSTRACT

The Early Mississippian (Tournaisian) positive $\delta^{13}C$ excursion (or TICE) is one of the largest recorded in the Phanerozoic and the organic carbon (OC) burial associated with its development is hypothesized to have driven global cooling and increased glaciation. We are testing the hypothesis that expanded ocean euxinia/anoxia drove widespread OC burial and the TICE and we are testing this hypothesis using uranium isotopes ($\delta^{238}U$) of Lower Mississippian marine limestones from southern Nevada as a global seawater redox proxy.

$\delta^{238}U$ trends record a prominent mid-Tournaisian negative excursion (~0.30‰ magnitude) lasting ~1 My. The lack of correlation among $\delta^{238}U$ values and water-depth dependent facies changes, terrestrial influx proxies (Al, Th, wt% carbonate), redox-sensitive metals (U, V, Mo, Re) and diagenetic proxies (Mg/Ca, Mn/Sr) suggests that the $\delta^{238}U$ curve represents a global seawater redox signal. The negative $\delta^{238}U$ excursion

(indicating increased sediment deposition under oxygen-depleted conditions) is coincident with the onset and peak of the first TICE positive excursion supporting the hypothesis that expanded ocean euxinia/anoxia controlled OC burial, we term this the Tournaisian oceanic anoxic event or TOAE. These results provide the first evidence from a *global* redox proxy that widespread ocean euxinia/anoxia controlled Tournaisian OC burial and enhanced long-term global cooling/glaciation. U modeling results indicate that during the TOAE, the area of euxinic/anoxic seafloor increased by 6x and that the negative $\delta^{238}U$ excursion was initially driven by euxinic conditions which waned and was replaced by anoxic/suboxic conditions where OC burial continued, but there was low U fractionation/sequestration. Comparisons between modeled OC burial amounts of the TICE versus the Late Ordovician (Hirnantian) positive $\delta^{13}C$ excursion (HICE), which occurred during peak Gondwanan glaciation, indicates that substantially more OC was buried during the TICE and adds strong support that the TOAE ultimately enhanced Tournaisian global cooling and increased glaciation.

In contrast to most Paleozoic and Mesozoic OAEs, the TOAE developed during (and further enhanced) long-term late Paleozoic global cooling. We interpret that the TOAE developed in response to this long-term cooling, which intensified atmospheric and ocean circulation, enhanced upwelling- and eolian-derived nutrient flux, increased productivity and dissolved O_2 consumption, which lead to ocean euxinia/anoxia expansion.

TABLE OF CONTENTS

Introduction 1
Geological and geochemical background 4
Mississippian paleogeography, western U.S. tectonics, and paleoclimate 4
Lower Mississippian stratigraphy, southern Nevada 5
Carbon and oxygen isotopes 6
Uranium isotopes systematics in limestones 8
Redox sensitive metals 10
Methods 12
Results 15
Stratigraphic results 15
Geochemical results 17
Uranium isotopes 17
Carbon isotopes 17
Major and trace elements 18
Discussion 19
Evaluating global signal of $\delta^{238}U$ curve 19
Quantifying U and C isotopic excursions 22
$\delta^{238}U$ vs $\delta^{13}C$ temporal relationships 28
Tournisian ocean anoxia and climate 30
Conclusions 34
References 36
Figures 48
Tables 55

Introduction

Large, repeated-positive carbon isotope ($\delta^{13}C$) excursions are a common feature in Precambrian through Phanerozoic marine carbonates and organic matter (e.g., Veizer et al., 1999; Knoll, 2000; Saltzman, 2005; Bachan et al., 2017; Zhou et al., 2017). These positive excursions are attributed to the increase in the burial fraction of organic carbon (OC) produced by oxygenic photosynthesis and results in the withdrawal of CO_2 from the atmosphere (and climatic cooling) and the buildup of pO_2. In addition to influencing atmospheric chemistry, large positive $\delta^{13}C$ excursions are associated with several of the 'big five' mass extinctions (e.g., Joachimski and Buggisch, 1993; Ghienne et al., 2014) highlighting the fact that positive $\delta^{13}C$ excursions record key processes and events in Earth history. The cause(s) of OC burial events generating positive $\delta^{13}C$ excursions are attributed to increases in primary productivity, decreases in dissolve seawater O_2, or increased sedimentation rates (Scholle and Arthur, 1980); however, distinguishing among these potential drivers is not straightforward leading to competing or ambiguous paleoenvironmental interpretations involving global or local processes. Traditional tools used for deciphering which mechanism(s) best explains the origin of particular OC burial events include lithologic and paleobiologic features, trace element geochemistry, Fe speciation, and S- and N-isotopes (e.g. Meyer and Kump, 2008); however, these tools reflect local rather than global processes.

Uranium (U) isotopes of marine carbonates can provide an estimate of globally-integrated ocean redox conditions, therefore it can distinguish among the causes of OC

burial and resultant positive $\delta^{13}C$ excursions. U-isotopes are a global proxy because the ocean residence time of U is significantly longer (~400 ky; Dunk et al., 2002) than ocean mixing times, and U isotopes fractionate during the reduction of soluble U(VI) to insoluble U(IV) (Bigeleisen, 1996; Schauble, 2007; Weyer et al., 2008).

We apply the U-isotope redox tool to the one of the largest and longest lived positive $\delta^{13}C$ excursion in the Phanerozoic (Saltzman, 2005)—the Early Mississippian (Tournaisian) $\delta^{13}C$ isotope excursion or TICE, which is associated with a positive oxygen isotope ($\delta^{18}O$) shift and climate cooling (Mii et al., 1999; Saltzman, 2002; Saltzman et al., 2004; Buggisch et al., 2008; Qie et al., 2010; Yao et al, 2015; Maharjan et al., 2018a). Previous TICE studies interpreted that OC burial generating the excursion was the result of OC sequestration in thick successions of Lower Mississippian foreland basin deposits of western North America (i.e., a tectonic/sedimentation driver; Saltzman et al., 2000; 2004), and/or due to widespread oxygen minimum zone (OMZ) expansion (i.e., depleted O_2 driver; Yao et al., 2015; Maharjan et al., 2018b; Liu et al., 2018). The tectonic/sedimentation interpretations are based on timing relationships between the TICE and foreland basin evolution and model results, whereas the depleted O_2 interpretations are based mainly on anoxic sediment deposition (Buggisch et al., 2008), positive N-isotope (Yao et al., 2015; Maharjan et al., 2018; Liu et al., 2018) and positive $\delta^{34}S_{CAS}$ shifts (Maharjan et al., 2018b). To test which of these interpretations was responsible for the TICE organic carbon burial, we analyzed for U- and C-isotopes from Tournaisian limestones of southern Nevada to generate a global seawater redox curve.

The specific goals of the research are to 1) describe and interpret Early Mississippian (mid-Tournaisian) U- and C- isotope trends, 2) model the U and C isotope trends to estimate the pattern and extent of oxygen depletion and OC burial, and 3) discuss relationships of seawater redox trends and Early Mississippian climate change.

Geological and geochemical background

Mississippian paleogeography, western U.S. tectonics, and paleoclimate

The North American continent was located at tropical to subtropical paleolatitudes during the Early Mississippian and was rotated ~30° clockwise relative to the modern continental arrangement (Fig. 1A; Blakey, 2013). Convergence of western North America with a volcanic arc during the Late Devonian to Early Mississippian led to thrusting of deeper marine deposits over shallower marine deposits and the formation of the Antler foreland basin extending from Nevada north to Canada (Fig. 1C; Giles, 1996). Up to 500 m of Early Mississippian deep through shallow marine and non-marine siliciclastics and carbonate deposits accumulated within the foreland basin and above a thick succession of Proterozoic-Upper Devonian passive-margin deposits (Stewart and Poole, 1974; Goebel, 1991). The targeted Lower Mississippian limestone succession represents deposition in the carbonate-dominated portion of the Antler foreland basin during active convergent-margin tectonics.

The late Paleozoic ice age (LPIA) was traditionally characterized by a single, protracted (>75 My) glacial interval beginning in the Late Mississippian and lasting until the Early Permian (Veevers and Powell, 1987). More recently, studies indicate that the LPIA began earlier, ended later, and was characterized by repeated My-scale cycles of glacial ice expansion and contraction which grew from several ice centers (Isbell et al., 2003; Fielding et al., 2008; Montañez and Poulsen, 2013). While it is recognized that Gondwanan glaciation began at least by the Late Devonian (Famennian; Caputo et al,

2008; Isaacson et al., 2008), the pattern of cooling and glaciation before the Famennian and in the >15 My interval between the Famennian and well-documented Late Mississippian portion of the LPIA are not well understood.

Cooling and glaciation beginning in the Early Mississippian (Tournaisian) is supported by the occurrence of major incised valleys and sequence boundaries (related to glacio-eustatic sea-level fall) in North America, Saudi Arabia, Europe, Russia, and China (Kammer and Matchen, 2008 and references therein), the age of South American glacial deposits (Caputo et al, 2008), the development of orbital-scale sedimentary cycles related to Milankovitch glacio-eustasy (Elrick and Read, 1991; Wallace and Elrick, 2014), and prominent Tournaisian positive $\delta^{13}C$ and $\delta^{18}O$ shifts (Bruckschen and Veizer, 1997; Mii et al., 1999; Saltzman, 2002; Saltzman et al., 2004; Buggisch et al., 2008). Alternatively, a Middle to Late Mississippian (Visean-Serpukovian) LPIA onset is suggested by the age of glacial deposits in Australia and South America (González, 2001; Limarino et al., 2006; Fielding et al., 2008; Gulbranson et al., 2010), glacio-eustatically generated cyclothems (Bishop et al., 2009; Waters and Condon, 2012), climatically controlled changes in Gondwanan floral communities (Iannauzzi and Pfefferkorn, 2002), and a positive excursion of $\delta^{13}C$ and $\delta^{18}O$ (Mii et al., 1999; Buggisch et al., 2008; Giles, 2012).

Lower Mississippian stratigraphy, southern Nevada

In the Pahranagat Range of southern Nevada, the Lower Mississippian (Tournaisian) Joana Limestone and Limestone X unconformably overlie the Upper

Devonian Pilot Shale and conformably underlie the Middle Mississippian Chainman Shale (Fig. 3). The Joana Limestone (~85 m thick) is composed dominantly of shallow subtidal crinoidal grainstone and packstone facies representing middle to proximal carbonate ramp environments (Singler, 1987; Saltzman, 2002; Maharjan et al., 2018a; Table 1). The overlying Limestone X (~185 m thick) is composed dominantly of lime mudstone and skeletal wackestone representing outer to middle carbonate ramp environments (Maharjan et al., 2018a; Table 1). The stratigraphic transition from the Upper Devonian unconformity, the Joana Limestone, and the overlying Limestone X represents Tournaisian transgression related to 2nd- order eustatic sea-level rise (Johnson et al., 1985; Giles, 1996). The Joana Limestone and Limestone X span part of the *Siphonodella crenulata* - *Siphonodella isosticha* through Lower *Gnathodus typicus* conodont zones and occurs between ~355 Ma and 350 Ma (Fig. 2; Singler et al, 1987; Davydov et al., 2012; Maharjan et al., 2018a).

Carbon and oxygen isotopes

A prominent Early Mississippian (mid-Tournaisian) positive carbon isotope excursion is reported from North America, Europe, Russia and China (Saltzman, 2002; Saltzman et al., 2004; Katz et al., 2007; Buggisch et al., 2008; Qie et al., 2010; Yao et al., 2015) and has been termed the mid-Tournaisian carbon isotope excursion or TICE (Bruckschen and Veizer, 1997; Mii et al., 1999; Saltzman, 2002; Saltzman et al., 2004; Yao et al., 2015). With a magnitude of up to ~7‰, it is one of the largest positive carbon isotope excursions reported in the Phanerozoic (Saltzman, 2005; Buggisch et al., 2008).

Associated with the TICE is a positive $\delta^{18}O$ shift of ~1.5‰ (Bruckschen and Veizer, 1997; Mii et al., 1999; Buggisch et al., 2008). The TICE spans the *Siphondella isosticha* and *Gnathodus typicus* conodont zones and has an estimated duration of ~2-4 Ma (Fig. 2; Mii et al., 1999; Saltzman, 2002; Saltzman et al., 2004; Buggisch et al., 2008).

Although the TICE is documented globally, excursion patterns and magnitudes vary at the local and global scale. In North America, the magnitude of isotopic shift ranges from ~6.0‰ to ~7.0‰ (Saltzman, 2002; Saltzman, 2003; Katz et al., 2007) and several locations in Nevada (including this study), Utah, and Wyoming record a 'double spike' whose trough occurs near the *Siphondella isosticha* and *Gnathodus typicus* conodont zonal boundary (Saltzman, 2002; Saltzman, 2003; Katz et al., 2007). The Belgium and Russian TICE have magnitudes of 4-6‰, but only the Belgium records a double spike pattern (Saltzman et al., 2004). The lack of the double spike pattern in some North American and Russian locations may be the result of internal unconformities (Maharjan et al., 2018a), low sample resolution (Saltzman et al., 2004), or local processes (Katz et al., 2007).

The TICE is most commonly attributed to increased organic carbon burial (Bruckschen and Veizer, 1997; Mii et al., 1999; Saltzman, 2002; Saltzman et al., 2003, 2004; Buggisch et al., 2008) which could be the result of increased sedimentation rates, enhanced ocean primary productivity, and/or widespread ocean anoxia (Scholle and Arthur, 1980; Stein, 1986; Arthur et al., 1987; Arthur et al., 1988; Kump et al., 1999). The associated positive $\delta^{18}O$ is interpreted to represent cooling and continental glaciation

related to the drawdown of atmospheric CO_2 during organic matter burial (Bruckschen and Veizer, 1997; Mii et al., 1999; Saltzman, 2002; Saltzman et al., 2004; Buggisch et al., 2008).

Uranium isotopes systematics in limestones

It is important to highlight the difference between using U-isotopic signatures from carbonate versus siliciclastic deposits for seawater redox studies. Unlike modern limestones, Paleozoic limestones were mainly formed by carbonate-secreting benthic invertebrates and microbial communities living in water depths of less than a few tens of meters (James et al., 2010). These shallow-water particles were reworked and transported offshore by gravity-flow, storm, and tidal currents and accumulated as fine detrital lime mud- and silt-size particles. Once deposited, they were cemented directly on the seafloor and/or in shallow through deep burial diagenetic environments. This history implies that even though the fine detrital carbonate particles accumulated in fully oxygenated to poorly oxygenated deeper waters, their authigenic U component (minus any early and late diagenetic cements) was originally derived from well-oxygenated shallow-water environments. In contrast, fine siliciclastic deposits (i.e., shales) accumulating in offshore environments obtain their authigenic U component from offshore bottom waters (or porewaters) and original magmatic/metamorphic sources; therefore their U isotopic signature reflects local conditions that may not reflect global seawater signatures.

The studied Lower Mississippian limestones include offshore through shallow subtidal deposits; the finer grained offshore deposits were sourced from well oxygenated shallow subtidal deposits originally located in Utah/Arizona (Giles and Dickinson, 1995). Given the original oxygenated source for the offshore deposits, the redox signature provided by the U isotopes may or may not match those interpreted from their depositional redox characteristics that were interpreted using grain size, bioturbation intensity, presence/absence of benthic skeletal material, sedimentary structures, and organic matter content.

The major source of uranium in ocean is from weathering of the continental crust and the main sinks are suboxic-anoxic continental margin sediments, altered ocean crust and biogenic carbonates (Morford and Emerson, 1999; Weyer et al., 2008; Tissot and Dauphas, 2015). In oxic seawater, uranium exists mainly as U(VI) in the soluble form of uranyl (UO_2^{2+}) and binds with carbonate ions, forming $UO_2(CO_3)_3^{4-}$. Under anoxic conditions, uranium is microbially or abiotically reduced to insoluble U(IV) species and adsorbed by organic-metal ligands in humic acids or precipitation as uranium-rich minerals (uraninite) and is consequently removed from seawater (Barns and Cochran, 1990; Klinkhammer and Palmer, 1991; Hua et al., 2006; Morford et al., 2009; Romaniello et al., 2013). During reduction of U(VI) to U(IV), the larger ^{238}U nucleus is preferentially concentrated into the reduced U species due to the nuclear volume effect (Bigeleisen, 1996; Schauble, 2007). As a consequence, during times of expanding ocean euxinia/anoxia, more uranium is reduced to U(IV) and ^{238}U is sequestered into

euxinic/anoxic sediments leaving seawater enriched in ^{235}U, so that calcite and aragonite precipitating from the seawater will record lower $^{238}U/^{235}U$ ratios. Because the residence time of U (400±120ky) is significantly longer than ocean mixing times (Dunk et al., 2002), U isotopes in limestones should record global seawater redox conditions (e.g. Weyer et al., 2008; Brennecka et al., 2011; Dahl et al., 2014; Lau et al., 2016; Elrick et al., 2017).

U isotope ratios are reported as：

$$\delta^{238}\mathrm{U} = \left[\frac{(^{238}\mathrm{U}/^{235}\mathrm{U})_{sample}}{(^{238}\mathrm{U}/^{235}\mathrm{U})_{standard}} - 1\right] \times 1000‰$$

where the standard is CRM-145, which has a $^{235}U/^{238}U$ ratio of 0.0072543 ± 0.0000040 (New Brunswick Laboratory, 2008).

Redox sensitive metals

The solubility of redox sensitive metals (RSMs) including U, V, and Mo in seawater is controlled by redox conditions. These trace elements are soluble in oxic seawater and insoluble in anoxic or euxinic conditions resulting in sequestration into sediments underlying oxygen-depleted bottom waters (Tribovillard et al., 2006). If the area of anoxic seafloor expands, more RSMs are sequestered into detrital sediments leaving seawater relatively depleted and limestone precipitating from the seawater also RSM depleted (Algeo and Lyons, 2006). Therefore, selected RSM concentrations in limestones can reflect the redox information over a larger areal extent; whereas RSM concentrations in the detrital fraction represent more local signals unless coupled with

coeval deposits from widespread locations. RSMs can also be incorporated into secondary calcite cements during diagenesis, particularly if pore waters are oxygen depleted; therefore RSMs measured in bulk carbonates may reflect local diagenetic signals.

Methods

The Lower Mississippian Joana Limestone and Limestone X were measured and described on a bed-by-bed basis in the Pahranagat Range of southern Nevada (Fig. 3). Facies and corresponding depositional environments were interpreted using lithology, grain size, sorting, sedimentary structures, skeletal and trace fossil content, bed geometries, and facies associations. Facies stacking patterns were utilized to construct a sequence stratigraphic framework shown in Figure 3.

Samples and individual skeletal grain samples were collected every 2-4 m throughout the 245 m-thick section. To evaluate the effects of isotopic differences between primary skeletal calcite (representing original or near-original seawater values) versus coeval bulk limestone matrix (representing a combination of original seawater and diagenetic carbonate phases), individual corals, brachiopods, or crinoids were sampled and compared to coeval bulk limestone matrix.

Bulk limestone samples were chipped into small fragments that were free from secondary carbonate veins and weathering and were powdered with a Spex 8510 shatterbox in an alumina puck pulverizer. Skeletal fragments were drilled and the powder was collected for geochemical analyses.

All powdered samples were digested using ~50mL trace metal-free 1M HNO_3. The purpose of using this relatively strong acid is to release all the uranium in the bulk carbonate and prevent potential fractionation occurring during partial dissolution of

various secondary carbonate phases (cements) and back absorption of U onto undissolved phases such as clay and other undissolved minerals. During early diagenesis, uranium hosted by primary carbonate could be released due to dissolution and recrystallization and incorporated into secondary carbonate phases such as carbonate cements and carbonate fluorapatite, or the liberated U could have been reduced to U(IV) in anoxic porewaters. Incomplete carbonate dissolution might result in equilibrium uranium isotopic fractionation between the different phases and produce isotopic offsets. On the other hand bulk carbonate measurements could yield coherent stratigraphic trends in ancient carbonates (Zhang et al., 2018a). Therefore it is necessary to use relatively strong acid to prevent inconstant isotopic offset by the incomplete release of carbonate-hosted uranium.

For trace element and U isotopic analysis, ~1.5 grams of powder was dissolved with 50mL trace metal-free 1M HNO_3. Dissolved samples were centrifuged to remove solid insoluble residues. A split of the solution was diluted to keep Ca concentrations lower than 200 ppm to ensure high analytical precision of the quadrupole ICP-MS. The trace elements concentrations were measured on an iCAP-Q quadrupole ICP-MS at Arizona State University (W.M. Keck Foundation Laboratory for Environmental Biogeochemistry). The remaining sample solution was spiked using IRMM-3636 ^{233}U-^{236}U double spike (Verbruggen et al., 2008) following a ratio of 8.8 ng of spike/500 ng U in each sample. Spiked samples were transferred to Teflon vials and treated with 32wt% H_2O_2 and 15.6M HNO_3 three times on a hot plate for 2 hours to digest organic matter.

After digestion, samples underwent column chemistry to isolate and collect U following the UTEVA resin method (Weyer et al., 2008). The collected U solution was treated with 0.2ml 32wt% H_2O_2 and 1ml 3M HNO_3 twice to remove any organic matter contamination from the UTEVA resin. Before $\delta^{238}U$ analysis, a second automated column chemistry was used to remove traces of Na and Fe using the ESI PrepFast-MC system. Samples were loaded onto 1mL of Eichrom DGA resin in 6M HNO_3 and the sample matrix was eluted with 10 mL of 6 HNO_3 before eluting the U with 10 mL of 0.05 M HCl. Dried samples were subsequently redissolved and were analyzed for U isotope on a Thermo Neptune MC-ICP-MS at Arizona State University.

Carbon and oxygen isotopes analysis was conducted following the Spotl and Vennemann (2003) method. About 0.5mg of powdered sample was loaded into 12 mL borosilicate tubes, flushed with He, then reacted with H_3PO_4 at 50°C for 12 hours. The CO_2 converted from the carbonate sample was measured for $\delta^{13}C$ and $\delta^{18}O$ values using continuous flow Isotope Ratio Mass Spectrometry with a Gasbench device coupled to a Thermo Fisher Scientific Delta V Plus Isotope Mass Spectrometer at the UNM Center for Stable Isotopes. The results are reported using the delta notation, versus V-PDB. Reproducibility was better than 0.1‰ for both $\delta^{13}C$ and $\delta^{18}O$ based on repeats of a laboratory standard (Carrara Marble). The laboratory standards were calibrated versus NBS 19, for which the $\delta^{13}C$ is 1.95‰ and $\delta^{18}O$ is -2.2‰.

Results

Stratigraphic results

We identify 4 different facies within the studied section which are described in Table 1 and interpreted below. The dark lime-mudstone facies is interpreted to represent deposition in moderately to poorly oxygenated waters within offshore to lower shoreface environments along the outer ramp. The relative oxygen levels are interpreted from the occurrence of sparse benthic skeletal material (brachiopods, crinoids, tabulate corals) and sparse bioturbation (including Zoophycus and Chondrites trace fossils), dark color. Offshore to lower shoreface conditions are interpreted from the preserved suspension laminations, fine graded beds, and association with adjacent offshore to lower shoreface facies. A ~7 m interval (between 80-87 m) is characterized by very few benthic and trace fossils suggesting a brief period of poorly oxygenated conditions (but enough oxygen to support limited animal life). The wackestone-lime mudstone facies is interpreted to represent deposition under well to moderately oxygenated waters within lower shoreface environments of the outer to middle ramp. These oxygenation conditions are based on abundance of benthic skeletal and trace fossils and relatively dark color, while lower shoreface environments are interpreted from the common graded beds, lenticular bed geometries, abraded skeletal-grain fossils, and association with adjacent offshore facies. The skeletal wackestone facies is interpreted to represent deposition under well oxygenated waters within lower shoreface environments of the middle ramp. These oxygenated conditions are based on

the abundance of skeletal fossils and bioturbation, and the light gray color. The lower shoreface environments are interpreted from the common graded beds, abraded grains and association with adjacent offshore-lower shoreface facies. The crinoidal packstone facies is interpreted to represent deposition under fully oxygenated waters within upper shoreface environments of the inner ramp. The oxygenated conditions are interpreted from the abundance of skeletal grains and bioturbation, and the light color. The upper shoreface environments are interpreted from grain-supported texture, large grain size and abrasion and association with adjacent lower shoreface facies.

Eleven depositional sequences (~20-30 m thick) are recognized based on facies stacking patterns (Fig. 3). Transgressive systems of tracts (TST) of the Joana Limestone sequences are characterized by progressive upward deepening from crinoidal packstone to skeletal wackestone facies. Maximum flooding zones (MFZ) are comprised of skeletal wackstone facies, and highstand systems tracks (HST) are typified by upward shallowing successions of skeletal wackstone to crinoidal packstone facies. Sequences within Limestone X are characterized by TST composed of skeletal wackstone to lime mudstone facies, MFZ are composed of meter-thick intervals of lime mudstone/skeletal wackstone, and HSTs are characterized by skeletal wackstone to crinoidal packstones. Sequence boundaries in both the Joana and Limestone X are defined at the top of the shallowest water facies immediately before abrupt deepening trends related to the overlying TST. No evidence of subaerial exposure is observed in the field (karsting,

brecciation, paleosols) indicating relatively continuous deposition throughout the duration of the studied succession.

Geochemical results

Uranium isotopes

Uranium isotopes values range from -1.02‰ to 0.02‰ (Table 4) and are shown as a LOWESS-smoothed curve in Figure 3. All 58 samples were measured twice with a mean 2σ (2SD, N=85) of 0.08‰. The measurement of CRM-145 standard yields an average 2σ of 0.04 indicating good precision throughout the analytical session. The measurement of CRM-129a standard yields the average value of -1.69±0.09‰ (2SD, N=12) which is in agreement with previous work (Chen et al., 2018; Zhang et al., 2018b), indicating our measurement is accurate. $\delta^{238}U$ trends begin with high values (average -0.26‰) in lower and middle Joana Limestone, then gradually shift to lower values in upper Joana Limestone reach a low (~-0.6‰) at the base of Limestone X, then gradually shifts back to higher values in lower Limestone X and remains relatively stable throughout the middle and upper part of Limestone X. The negative $\delta^{238}U$ excursion has a magnitude of change of ~0.30‰ and spans about 65 meters of stratigraphy.

Carbon isotopes

Carbon isotope ($\delta^{13}C_{carb}$) values ranges fom -1.1‰ to 7.0‰ (Fig. 3, Table 4). $\delta^{13}C$ trends begin at about 0.0‰, then increase to ~2.5‰ and remain relatively stable throughout the majority of the Joana Limestone. This is followed by a prominent

positive shift which peaks at ~7‰, a brief negative 3.0‰ shift, a return to ~7‰ values ('double peak'), then a gradual negative ~5‰ shift across the upper half of Limestone X.

Major and trace elements

Cross plots of $\delta^{238}U$ values against proxies of local redox conditions (U, V, Mo), detrital influx (Al, Th, Fe, carbonate wt %), nutrients (Fe, P) and diagenesis (Mn/Sr, Mg/Ca, $\delta^{18}O$) are shown in Figure 4. No-covariation between $\delta^{238}U$ and these proxies is observed (Fig. 4; Table 4), suggesting that $\delta^{238}U$ values are not systematically altered from seawater values. Plots of selected elemental and isotopic concentration including Al, Th, Fe, and $\delta^{18}O$ versus stratigraphic thickness highlight changes occurring between 40 m and 60 m (Fig. 5).

Discussion

Evaluating global signal of $\delta^{238}U$ curve

We utilize a range of sedimentologic, stratigraphic, and geochemical proxies to evaluate potential local depositional and diagenetic influences on the measured $\delta^{238}U$ trends.

Several lines of sedimentologic and stratigraphic evidence argue against local depositional conditions controlling $\delta^{238}U$ trends. First, each of the poorly to well oxygenated facies record a wide range in $\delta^{238}U$ values; for example, the lime mudstone facies deposited under moderately to poorly oxygenated conditions records the same spread of isotopic values as the most oxic crinoidal packstone facies (Fig. 4). Second, the gradual negative $\delta^{238}U$ shift (indicating increased area of reducing sediment accumulation) at the top of the Joana Limestone occurs in a relatively monotonous succession of well oxygenated crinoidal packstones, whereas the shift back to higher values (indicating increased area of oxygenated sediment accumulation) occurs within a mix of poor, moderate, to well oxygenated facies (Fig. 3). Third, the complete negative $\delta^{238}U$ excursion continues across two prominent sequence boundaries indicating water-depth changes and associated environmental shifts did not influence the isotopic trends (Fig. 3).

We estimate the fraction of authigenic uranium in samples to evaluate whether the measured $\delta^{238}U$ values are derived from authigenic versus detrital phases using the U enrichment factor (UEF) from:

$$UEF = (U_{sample}/Al_{sample}) / (U_{PAAS}/Al_{PAAS})$$

where UEF is the U enrichment factor of samples, U_{sample} and Al_{sample} are U and Al concentrations, and U_{PAAS} and Al_{PAAS} are U and Al concentrations of Post-Archaean average shale (McLennan, 2001). UEF values >1 represent higher enrichment of uranium relative to shale (i.e., higher than average detrital U values; Morford and Emerson, 1999; Piper and Perkins, 2004; Tribovillard et al., 2006). Early Mississippian UEFs range from 21 to 1182, with an average of 438. This range and average is significantly >1, which supports the hypothesis that most of the measured uranium is authigenic rather than detrital (Fig.5).

To evaluate the influence of local detrital sediment or riverine water input on measured isotopic trends, we compare $\delta^{238}U$ values with Al, Th, and carbonate weight percentage values (% carb; Fig. 4). No correlation among these proxies is observed indicating the measured $\delta^{238}U$ trends were not influenced by these local processes. Al, Th, Fe stratigraphic profiles increase and UEF decreases at around ~70m, indicating increased terrestrial flux (Fig. 5).

We evaluate the potential effects of local oxygen-poor bottom water or porewaters by comparing $\delta^{238}U$ versus RSM (carbonate fraction), and Mn/Sr. The lack of co-variation among these redox proxies indicates that the $\delta^{238}U$ values were not controlled by enrichment of uranium in secondary carbonate phases precipitated in anoxic bottom water/porewater during early diagenesis (Fig. 4). In addition, all samples

have Mg/Ca values lower than 0.05 indicating they have not been dolomitized (Fig. 4). Phosphorus concentration increases at ~40m, probably indicating P regeneration due to anoxia in nearby basin (Fig.5).

The $\delta^{238}U$ values between skeletal grains (brachiopods, rugose coral, crinoids) versus coeval bulk matrix are within error of each other (Table 4). These results differ from those reported in earlier studies wherein bulk matrix values were enriched compared to their coeval skeletal grains (Bartlett et al., 2018; White et al., 2018). These results suggest that either the secondary cements in the bulk matrix were precipitated in well oxygenated porewaters in communication with the overlying seawater or that skeletal grains were diagenetically altered (isotopically enriched) similar to that of the bulk matrix. Skeletal grain alteration may be the result of the transformation from high- to low-Mg calcite (crinoids), inclusion of intra-septa cements of rugose coral samples, or recrystallization of originally low-Mg calcite (brachiopods).

We assume that the $\delta^{238}U$ values of bulk carbonate samples (and coeval skeletal grains) were isotopically enriched by secondary cements precipitated in poorly oxygenated pore waters (Romaniello et al., 2013, Chen et al., 2018). The study of Neogene Bahamas carbonates suggests that early diagenesis fractionate $\delta^{238}U$ by an average of 0.27±0.14‰ offset heavier than coeval seawater (Chen et al., 2018). However, the locally weighted scatter plot smoothing (LOWESS) method could minimize the effect of this random early diagenetic enrichment and reveal the secular relative variation of $\delta^{238}U$ (Chen et al., 2018; Fig. 3). Despite the assumed diagenetic enrichment,

we argue that the samples were altered relatively uniformly throughout the succession, regardless of facies, based on their nearly invariant $\delta^{18}O$ (average = -4.0‰) and Mn/Sr values (~0.1; diagenesis tends to enrich carbonates in Mn and deplete them in Sr due to their different distribution coefficients during the calcite-water exchange (Fig. 4; Banner and Hansen, 1990). Given results from combined lithologic, stratigraphic, and geochemical results, we interpret that the observed $\delta^{238}U$ isotopic trends represent relative changes in global seawater redox conditions and we identify the prominent negative excursion as a Tournaisian ocean anoxic event or TOAE.

Quantifying U and C isotopic excursions

We estimate the duration of the U- and C-isotopic excursions using conodont biostratigraphy tied to the radiometric time scale. Using the zonal-level numeric age control reported in Buggisch et al. (2008; based on the STG 2002), the duration of the TICE in the study area is ~ 4 My and the TOAE is ~1 My. This TICE duration is slightly longer but still consistent with estimates reported from previous studies (2 My; Saltzman et al., 2004; 2-4 My; Maharjan et al., 2018b).

The onset and the peak of the $\delta^{238}U$ excursion or TOAE coincides with the onset and first peak of the $\delta^{13}C$ excursion (TICE; Fig. 3). This temporal relationship clearly supports the hypothesis that increased ocean euxinia/anoxia enhanced organic carbon burial driving the positive $\delta^{13}C$ shift. These results provide the first evidence from a *global* redox proxy that extensive Tournaisian OC burial and the resultant TICE event enhanced late Paleozoic long-term global cooling/glaciation.

We use a dynamic model to quantitatively estimate the flux of seawater U to euxinic/anoxic sediment sinks ($f_{eux\ flux}$) and the percent of euxinic/anoxic seafloor (f_{eux}) using a modified model of Lau et al. (2016) and the estimated TOAE duration.

The main source of U to oceans is from rivers and the main sinks are oxic/suboxic, anoxic, and euxinic sediment sinks (Tissot et al., 2015). We simplify the model into 2 sinks (oxic and euxinic sinks). The mass balance equation for the seawater U inventory and its isotopic composition (from Lau et al., 2016) is:

$$dN_u/dt = J_{river} - J_{eux} - J_{oxic} \quad (1)$$

$$N_u \times d\delta^{238}U_{seawater}/dt = J_{river} \times (\delta^{238}U_{river} - \delta^{238}U_{seawater}) - J_{eu} \times \Delta_{eux} - J_{oxic} \times \Delta_{oxic} \quad (2)$$

where N_{sw} is the ocean U reservoir in moles. $\delta^{238}U_{seawater}$ and $\delta^{238}U_{river}$ are U isotopic compositions of seawater and riverine flux. J values are U source and sink fluxes, respectively, introduced by river (J_{river}) and buried in euxinc (J_{eux}) and oxic (J_{oxic}) sediments. The cap delta notation (Δ) is used to express U fractionation between seawater and sediment. The uranium flux to sediments is a function of sediment area (A_{eux} and A_{oxic}) and U concentration in the ocean (N_u/V_{ocean}):

$$J_{oxic} = k_{oxic} \times A_{oxic} \times N_u/V_{ocean} \quad (3)$$

$$J_{eux} = k_{eux} \times A_{eux} \times N_u/V_{ocean} = k_{eux} \times A_{ocean} \times f_{eux} \times N_u/V_{ocean} \quad (4)$$

where k values are modern measured uranium burial rates (Table 2). The anoxic seafloor fraction (f_{eux}) can be expressed by:

$$f_{eux} = (J_{river} \times (\delta^{238}U_{river} - \delta^{238}U_{seawater}) - N_u \times d\delta^{238}U_{seawater}/dt) / (k_{eux} \times A_{ocean} \times N_u/V_{ocean}) \times \Delta_{eux} \quad (5)$$

The uranium anoxic flux fraction ($f_{eux\ flux}$) can be expressed by:

$$F_{eux\ flux} = J_{eux} / J_{total} = J_{eux} / (J_{oxic} + J_{eux}) = (k_{eux} \times A_{ocean} \times f_{eux} \times N_u/V_{ocean})/(k_{eux} \times A_{ocean} \times f_{eux} \times N_u/V_{ocean} + k_{oxic} \times A_{ocean} \times (1-f_{eux}) \times N_u/V_{ocean}) \quad (6)$$

Previous studies reported the effects of the diagenetic addition of isotopically heavy $\delta^{238}U$ from oxygen-depleted pore waters upon burial (Romaniello et al., 2013; Chen et al., 2018). To correct for this diagenetic offset in this model, we subtract the value of 0.27‰ (Chen et al., 2018) from our LOWESS-smoothed $\delta^{238}U$ curve.

In order to better quantify the influence the ocean euxinia/anoxia to seawater $\delta^{238}U$, we assume that the pre-TOAE oceanic uranium cycle was in steady state. The $\delta^{238}U$ profile corrected for diagenetic offset shows a significantly lower Early Mississippian seawater background value (~0.68‰) than today (-~0.39‰; Tissot et al., 2015), implying that the steady state U concentration in Early Mississippian ocean was different from today. Therefore, we use a steady state mass balance model (Montoya-Pino et al. 2010) to constrain the initial Early Mississippian U seawater conditions. The steady state mass balance equation for the seawater U inventory and its isotopic composition is:

$$\delta^{238}U_{river} = f_{eux\ flux} \times \delta^{238}U_{eux} + (1 - f_{eux\ flux}) \times \delta^{238}U_{oxic} \quad (7)$$

$$\delta^{238}U_{eux} = \delta^{238}U_{seawater} + \Delta_{eux} \quad (8)$$

$$\delta^{238}U_{oxic} = \delta^{238}U_{seawater} + \Delta_{oxic} \quad (9)$$

where $\delta^{238}U_{eux}$ and $\delta^{238}U_{oxic}$ are U isotopic compositions of anoxic/euxinc and oxic/suboxic sedimentary sinks, respectively. Combining equations 3 and 4 and (7-9), we solve for the euxinic/anoxic seafloor percentage (f_{eux}) and the oceanic reservoir (N_u) in steady state:

$$f_{eux} = \frac{\frac{\delta^{238}\mathrm{U}_{\mathrm{river}} - \delta^{238}\mathrm{U}_{\mathrm{seawater}} - \Delta_{\mathrm{oxic}}}{\Delta_{eux} - \Delta_{\mathrm{oxic}}} \times k_{oxic}}{k_{eux} - \frac{\delta^{238}\mathrm{U}_{\mathrm{river}} - \delta^{238}\mathrm{U}_{\mathrm{seawater}} - \Delta_{\mathrm{oxic}}}{\Delta_{eux} - \Delta_{\mathrm{oxic}}} \times (k_{oxic} - k_{eux})}$$

$$N_u = J_{riv}/(k_{eux} \times A_{ocean} \times f_{eux} + k_{oxic} \times A_{ocean} \times (1\text{-}f_{eux}))$$

With the initial steady state determined, we calculate trends of fractions of euxinic seafloor (f_{eux}), euxinic U flux ($f_{eux\ flux}$), and U oceanic reservoir size (N_u) using the dynamic model (Fig. 6).

The dynamic model results suggest that the percent euxinic/anoxic seafloor increases from a pre-TOAE average value of ~5% to ~30% during the peak TOAE and ~90% of U sinking flux was sequestered into euxinic/anoxic sediments during peak euxinia/anoxia (Figs. 6B, 6C). For comparison, the modern ocean is characterized by <0.5% euxinic/anoxic seafloor (Tissot et al., 2015 and references therein) and indicates that even prior to the TOAE, the Early Mississippian oceans had an order of magnitude

more euxinic/anoxic seafloor than today. Significantly more reducing Paleozoic oceans are indicated by results from previous $\delta^{238}U$-derived modeling studies (Song et al., 2017; White et al., 2018) and likely reflects the presence of expansive epeiric seas that accumulated widespread moderately to poorly oxygenated deeper subtidal deposits (e.g., Walker et al., 2002)

We estimate the amount of organic carbon (OC) buried during the studied interval and compare that amount to other time intervals characterized by high OC burial. Burial estimates are derived using the carbon cycle model of Arthur and Kump (1999; Table 3) and the observed $\delta^{13}C$ trends or percent changes in seafloor euxinia/anoxia determined from the dynamic model. OC burial estimates from the observed $\delta^{13}C$ start by expressing the seawater carbonate isotopic composition as:

$$d\delta_{carb}/dt = (F_w \times (\delta_w - \delta_{carb}) - F_{bcarb} \times \Delta_{carb} - F_{borg} \times (\Delta_{org}))/M$$

where δ_{carb} and M are the isotopic composition and marine dissolved organic carbon (DIC) reservoir size (assumed in steady state), respectively. Volcanism-metamorphism and weathering of silicate and carbonate rocks and organic matter are the major carbon sources into the oceanic inventory (F_w) and their average isotopic composition can be expressed as (δ_w). The burial of carbonate C (F_{bcarb}) and organic C (F_{borg}) into sediments is a major sink of carbon. Δ_{carb} and Δ_{org} are the isotopic differences between DIC-calcite and DIC-organic matter, respectively. In order to simplify the calculation, we assume

there is no fractionation during calcite precipitation (Δ_{carb}=0). The organic carbon burial flux derived from carbonate $\delta^{13}C$ curve can be expressed by:

$$F_{borg} = F_w \times (\delta_w - \delta_{carb}) - M \times d\delta_{carb}/dt$$

To estimate the OC burial based on model-calculated percent euxinic/anoxic seafloor (f_{eux}), we sum up the OC burial in oxic and euxinic/anoxic sediments caused by the TOAE:

$$F_{borg\ eux} = k_{borg\ oxic} \times A_{ocean} \times (1-f_{eux}) + k_{borg\ eux} \times A_{ocean} \times f_{eux}$$

where $F_{borg\ eux}$ is the estimated total oceanic OC burial, $k_{borg\ oxic}$ and $k_{borg\ eux}$ are OC burial rates in oxic and euxinic/anoxic sediments, respectively (Berner, 1982; Table 3).

The modeled OC burial event based on the $\delta^{13}C$ trends lasts ~4 My similar to the observed TICE. It also shows two burial peaks, both with of rates ~2.4×10^{16}mol/Ky (Fig. 7B). Integrating the amount of OC buried over the entire 4 My interval indicates a total OC burial of ~7.9×10^{19}mol (or ~9×10^{20} gC) which is similar to that calculated by Saltzman et al., (2004) for the same time interval. We compare this total Tournaisian OC burial amounts to the OC burial during Late Ordovician (Hirnantian) positive carbon isotope excursion (HICE; Kump et al., 1999), which occurs during peak Gondwanan glaciation. The HICE is over 10x shorter and of similar magnitude of the TICE, indicating total OC burial amount was substantially lower than during the TICE. The fact that HICE is associated with peak glaciation helps to support the hypothesis that mid-Tournaisian OC burial could have enhanced the cooling/glaciation.

OC burial estimated using f_{eux} from the dynamic U model indicates a peak value of ~3.7×10^{16}mol/Ky that lasts only ~1 My. The difference between OC burial amounts reflects the longer duration for the measured $\delta^{13}C$ curve vs the $\delta^{238}U$ curve and reiterates the temporal offset between the two isotopic excursions.

$\delta^{238}U$ vs $\delta^{13}C$ temporal relationships

Utilizing the OC burial amounts determined from the measured $\delta^{238}U$ curve (Fig. 7C), we use the Kump and Arthur (1999) model to generate a modeled $\delta^{13}C$ curve to compare to the measured curve (Fig. 7D). The timing and magnitude of the positive model $\delta^{13}C$ shift is similar to that of the observed first TICE peak; however, no second peak developed indicating it is not possible to generate the double peak pattern with a single OC burial event. The following section explores potential scenarios to explain this issue.

The second positive TICE peak implies that OC burial continued after the TOAE, however the coeval higher $\delta^{238}U$ values suggests waning euxinic conditions and a decrease in U fractionation and sequestration. This may be explained by a substantial drawdown of seawater U during the TOAE or by initial TOAE euxinic conditions replaced by anoxic or suboxic conditions.

Extensive and prolonged accumulation of sediments deposited under euxinic conditions will drawdown seawater U concentrations and it has been suggested that this could decrease U fractionation (Dahl et al., 2014). This argument is presumably based on

the fact that as more uranium is removed from the reservoir, kinetic U fractionation decreases and seawater $\delta^{238}U$ shifts to higher values regardless of ongoing euxinic/anoxic sediment accumulation. Such a scenario is supported by the fact that post-TOAE U concentrations (average ~0.25ppm) are 3x lower than pre-TOAE values (average ~0.7ppm; Figs. 6D, 6E) and measured U concentrations do not shift back to higher background as the U model predicts (Fig. 6D). Despite the differences in absolute values, the difference of relative variation of U concentration between model and observation probably implies that seawater U was depleted after TOAE. However, the lower post-TOAE U concentrations lie within the range reported for other post-anoxia events recorded in the Paleozoic and Mesozoic (Bartlett et al., 2018; White et al., 2018; Zhang et al., 2018a), therefore do not stand out as particularly low values. Future studies are required to compare U concentrations in coeval shales/mudrocks to determine if they record U depletion after the TOAE and to evaluate if U fractionation decreases under conditions of diminished U concentrations.

Ongoing OC burial resulting in the second TICE peak may have occurred under anoxic or suboxic (vs euxinic) conditions where minor U sequestration and fractionation occurs (~0.24‰ non-euxinic anoxic/hypoxic; Andersen et al., 2017, ~0.1‰ suboxic; Weyer et al., 2008). In this scenario, the onset of the TOAE negative excursion is interpreted to represent widespread euxinic conditions (with ~0.65‰ fractionation; Weyer et al., 2008), then after ~500 ky, euxinia wanes and is replaced by anoxic/suboxic conditions which lead to continued OC burial (and ongoing high $\delta^{13}C$ values), but a $\delta^{238}U$

shift back to higher values because of low U sequestration and fractionation. A change from early widespread euxinic followed by anoxic/suboxic conditions ~500 ky after the onset of TOAE implies that SO_4 reduction to H_2S (euxinia) ended and was replaced by ferric iron or nitrate reduction (Canfield and Thamdrup, 2009). This retreat of euxinic conditions at the first TICE peak may have occurred when atmospheric O_2 increased enough (due to OC burial) to oxygenate the oceans to suboxic/anoxic levels. Euxinia, rather than anoxia, generating the initial negative TOAE shift is supported by modeling results which indicate that anoxia alone would require greater than 90% of the seafloor under oxygen-depleted conditions; a condition that is not supported by the Early Mississippian stratigraphic and paleobiologic record (Ross and Ross; 1987; Davylov et al., 2012).

A similar shift from early euxinic to later anoxic/suboxic conditions has been suggested to explain the temporal offset between $\delta^{238}U$ and $\delta^{13}C$ trends for the Late Cambrian SPICE event (Dahl et al., 2014). This two-stage redox interpretation is supported by the record of a substantial SO_4 depletion associated with the redox transition, and they argue that under the new anoxic conditions, phosphorous regeneration supported ongoing elevated primary productivity, OC burial, and continued high $\delta^{13}C$ values.

Tournisian ocean anoxia and climate

The temporal coincidence between the negative $\delta^{238}U$ excursion and the initial positive $\delta^{13}C$ excursion provides the first evidence from a *global* redox proxy that

enhanced Tournaisian OC burial was driven by expanded ocean euxinia/anoxia and provides strong support that Early Mississippian cooling/glaciation was driven by this burial event. Previous studies interpreted expanded oxygen minimum zones (OMZ) drove OC burial and climate change (Saltzman et al., 2000; Saltzman et al., 2004; Yao et al., 2015; Maharjan et al., 2018b; Liu et al., 2018); however, OMZ expansion was interpreted from local ($\delta^{15}N$; Yao et al., 2015; Maharjan et al., 2018a and $\delta^{34}S_{CAS}$; Gill et al., 2007; Maharjan et al., 2018b), rather than global redox proxies.

In contrast to most Paleozoic and Mesozoic OAEs, the TOAE occurred during (and further enhanced) long-term cooling between the Devonian greenhouse and LPIA, and it adds to the growing list of OAEs developed during icehouse or cooling climates (Bartlett et al., 2018, White et al., 2018). We interpret that the TOAE developed in response to this long-term cooling (beginning at least by the Famennian), which increased latitudinal thermal gradients and intensified thermohaline circulation and meridional winds. Intensified ocean and atmospheric circulation enhanced upwelling- and eolian-derived nutrients leading to increased surface ocean productivity and dissolved O_2 consumption leading to widespread euxinia/anoxia expansion. Decreased deep-water O_2 concentrations during cooler climates is supported by recent reports investigating O_2 concentrations during the last two Pleistocene glacial stages (Hoogakker et al., 2014; Lu et al., 2016). In these studies, deep-water O_2 depletions are the result of the reorganization of high-latitude downwelling patterns leading to decreased North Atlantic deep water ventilation (Adkins et al. 2002; Howe et al., 2016) as well as the

strengthened efficiency of the global biologic pump leading to enhanced organic matter flux to deep oceans (Pedersen, 1983; Martin, 1990; Bradtmiller et al., 2010; Cartapanis et al., 2016). These combined processes clearly outweigh the effects of increased oxygen solubility related cooler glacial seawater temperatures.

Initial euxinia/anoxia development would provide a short-term positive feedback loop to continue cooling and ocean oxygen depletion due to additional OC sequestration and pCO_2 reduction. Part of the feedback loop includes the release of PO_4 from sediments lying beneath expanded anoxic bottom waters which resulted in enhanced surface water productivity and O_2 consumption (Ingall, 1993; Saltzman et al., 2004; Ingall et al., 2005; Algeo and Ingall, 2007). Liu et al. (2018) propose that the end of the feedback loop was due to Mississippian climatic cooling which eventually collapsed tropical ocean productivity leading to the end of anoxia expansion. This interpretation is not supported by reports that global OC burial rates were actually higher during Pleistocene glacial than during interglacial stages (Pedersen, 1983; Martin, 1990; Bradtmiller et al., 2010; Cartapanis et al., 2016). Instead, the end of the Mississippian positive feedback loop and OC burial was likely related to the eventual depletion of regenerated nutrients required to drive prolonged surface water productivity.

If this hypothesis is correct, there should be several ocean anoxic events during the LPIA following the recharge of nutrients and this is not observed. There are several possibilities explaining why the TOAE is a single ocean anoxic event during the transitional period into full glaciation including: 1) the eolian Fe input during the early

stage of the LPIA triggered massive primary productivity and depleted the surplus PO_4 accumulated before the LPIA, changing the ocean from Fe-limited to PO_4-limited state (e.g. Saltzman 2005), 2) cooling seawater temperatures limited nitrogen fixers in the surface ocean, making it hard to support enough productivity for widespread euxinia during full glaciation (Stal, 2009).

The ultimate driver for long-term, late Paleozoic global cooling has been interpreted as the result of 1) the expansion of wetland forests (leading to increased terrestrial carbon storage) and accelerated silicate weathering rates (Eyles, 1993; Montañez and Poulson, 2013), 2) enhanced silicate weathering rates related to orogenic uplifts (Veevers and Powell, 1987; Isbell et al., 2012; Goddéris et al., 2017) or lengthening of low-latitude volcanic arcs and ophiolite belts (MacDonald et al., 2019), 3) continental drift over polar regions, and 4) changing ocean circulation patterns related to opening or closure of oceanic gateways (i.e., Rheic ocean closure (Veevers and Powell, 1987; Smith and Read, 2000; Saltzman, 2000). Regardless of which mechanism(s) is/are responsible for this long-term cooling, OC burial due to euxinia/anoxia expansion enhanced the cooling trends.

Conclusions

1) $\delta^{238}U$ trends across a ~4 My succession of Lower Mississippian (Tournaisian) deep- through shallow-marine limestones in southern Nevada record a ~1 My-long negative $\delta^{238}U$ excursion with the magnitude of ~0.3‰. The lack of co-variation among $\delta^{238}U$ values and water-depth dependent facies changes, terrestrial influx proxies (Al, Th, wt% carb), redox-sensitive metals (U, V, Mo, Re) and diagenetic proxies (Mg/Ca, Mn/Sr) indicates that the $\delta^{238}U$ curve represents a global seawater redox signal and that the Tournaisisn negative excursion represents expanded euxinic/anoxic conditions (Tournaisian oceanic anoxic event or TOAE). U modeling results suggest a 6x increase in area of euxinic/anoxic seafloor and ~90% of U sinking flux was sequestered into euxinic/anoxic sediments during the peak TOAE.

2) The temporal coincidence between the TOAE and first peak of the global positive $\delta^{13}C$ excursion (TICE) provides the first evidence from a global redox proxy that enhanced Tournaisian OC burial was driven by expanded ocean euxinia/anoxia. These results provides strong support that Early Mississippian cooling/glaciation was driven by this burial event. The continuing positive $\delta^{13}C$ trends after the TOAE combined with modeling results suggest that euxinic conditions initiated the TOAE, then shifted to anoxic/suboxic conditions which prolonged organic carbon burial, but limited U fractionation/sequestration. Comparison between modeled OC burial amounts of the TICE versus the Late Ordovician (Hirnantian) positive carbon excursion (HICE), which occurred during major Gondwanan glaciation, indicates that substantially more carbon

was buried during TICE and supports the hypothesis that mid-Tournaisian OC burial enhanced global cooling and glaciation.

3) In contrast to most Paleozoic and Mesozoic OAEs, the TOAE developed during (and further enhanced) long-term late Paleozoic global cooling. We interpret that the TOAE developed in response to this long-term cooling, which intensified atmospheric circulation, intensified and modified ocean circulation, enhanced upwelling- and eolian-derived nutrients, increased surface ocean productivity and dissolved O_2 consumption, which lead to ocean euxinia/anoxia expansion.

References

Adkins, J.F., 2002, The Salinity, Temperature, and delta 18O of the Glacial Deep Ocean: Science, v. 298, p. 1769–1773, doi: 10.1126/science.1076252.

Algeo, T.J., and Lyons, T.W., 2006, Mo-total organic carbon covariation in modern anoxic marine environments: Implications for analysis of paleoredox and paleohydrographic conditions: Paleoceanography, v. 21, doi: 10.1029/2004pa001112.

Algeo, T.J., and Ingall, E., 2007, Sedimentary Corg:P ratios, paleocean ventilation, and Phanerozoic atmospheric pO2: Palaeogeography, Palaeoclimatology, Palaeoecology, v. 256, p. 130–155, doi: 10.1016/j.palaeo.2007.02.029.

Arthur, M.A., Schlanger, S.O., and Jenkyns, H.C., 1987, The Cenomanian-Turonian Oceanic Anoxic Event, II. Palaeoceanographic controls on organic-matter production and preservation: Geological Society, London, Special Publications, v. 26, p. 401–420, doi: 10.1144/gsl.sp.1987.026.01.25.

Arthur, M.A., Dean, W.E., and Pratt, L.M., 1988, Geochemical and climatic effects of increased marine organic carbon burial at the Cenomanian/Turonian boundary: Nature, v. 335, p. 714–717, doi: 10.1038/335714a0.

Bachan, A., Lau, K.V., Saltzman, M.R., Thomas, E., Kump, L.R., and Payne, J.L., 2017, A model for the decrease in amplitude of carbon isotope excursions across the Phanerozoic: American Journal of Science, v. 317, p. 641–676, doi: 10.2475/06.2017.01.

Banner, J.L., and Hanson, G.N., 1990, Calculation of simultaneous isotopic and trace element variations during water-rock interaction with applications to carbonate diagenesis: Geochimica et Cosmochimica Acta, v. 54, p. 3123–3137, doi: 10.1016/0016-7037(90)90128-8.

Barnes, C., and Cochran, J., 1990, Uranium removal in oceanic sediments and the oceanic U balance: Earth and Planetary Science Letters, v. 97, p. 94–101, doi: 10.1016/0012-821x(90)90101-3.

Bartlett, R., Elrick, M., Wheeley, J.R., Polyak, V., Desrochers, A., and Asmerom, Y., 2018, Abrupt global-ocean anoxia during the Late Ordovician–early Silurian detected using uranium isotopes of marine carbonates: Proceedings of the National Academy of Sciences, v. 115, p. 5896–5901, doi: 10.1073/pnas.1802438115.

Berner, R.A., 1982, Burial of organic carbon and pyrite sulfur in the modern ocean; its geochemical and environmental significance: American Journal of Science, v. 282, p. 451–473, doi: 10.2475/ajs.282.4.451.

Bigeleisen, J., 1996, Nuclear Size and Shape Effects in Chemical Reactions. Isotope Chemistry of the Heavy Elements: Journal of the American Chemical Society, v. 118, p. 3676–3680, doi: 10.1021/ja954076k.

Bishop, J.W., Montañez, I.P., Gulbranson, E.L., and Brenckle, P.L., 2009, The onset of mid-Carboniferous glacio-eustasy: Sedimentologic and diagenetic constraints, Arrow Canyon, Nevada: Palaeogeography, Palaeoclimatology, Palaeoecology, v. 276, p. 217–243, doi: 10.1016/j.palaeo.2009.02.019.

Blakey, R.C., 2013. Colorado plateau geosystems: http://deeptimemaps.com/wp-content/uploads/2018/07/NAM_key-345Ma_EMiss-th-min.jpg (accessed April 2019)

Blakey, R.C., 2016. Colorado plateau geosystems: https://deeptimemaps.com/wp-content/uploads/2016/05/340_Ma_Miss_GPT-1.png (accessed May 2019)

Bradtmiller, L., Anderson, R., Sachs, J., and Fleisher, M., 2010, A deeper respired carbon pool in the glacial equatorial Pacific Ocean: Earth and Planetary Science Letters, v. 299, p. 417–425, doi: 10.1016/j.epsl.2010.09.022.

Brennecka, G.A., Herrmann, A.D., Algeo, T.J., and Anbar, A.D., 2011, Rapid expansion of oceanic anoxia immediately before the end-Permian mass extinction: Proceedings of the National Academy of Sciences, v. 108, p. 17631–17634, doi: 10.1073/pnas.1106039108.

Bruckschen, P., and Veizer, J., 1997, Oxygen and carbon isotopic composition of Dinantian brachiopods: Paleoenvironmental implications for the Lower Carboniferous of western Europe: Palaeogeography, Palaeoclimatology, Palaeoecology, v. 132, p. 243–264, doi: 10.1016/s0031-0182(97)00066-7.

Buggisch, W., Joachimski, M.M., Sevastopulo, G., and Morrow, J.R., 2008, Mississippian δ13Ccarb and conodont apatite δ18O records — Their relation to the Late Palaeozoic Glaciation: Palaeogeography, Palaeoclimatology, Palaeoecology, v. 268, p. 273–292, doi: 10.1016/j.palaeo.2008.03.043.

Canfield, D.E., and Thamdrup, B., 2009, Towards a consistent classification scheme for geochemical environments, or, why we wish the term ‘suboxic’ would go away: Geobiology, v. 7, p. 385–392, doi: 10.1111/j.1472-4669.2009.00214.x.

Caputo, M.V., Melo, J.H.G.D., Streel, M., and Isbell, J.L., 2008, Late Devonian and Early Carboniferous glacial records of South America: Special Paper 441: Resolving the Late Paleozoic Ice Age in Time and Space, p. 161–173, doi: 10.1130/2008.2441(11).

Cartapanis, O., Bianchi, D., Jaccard, S.L., and Galbraith, E.D., 2016, Global pulses of organic carbon burial in deep-sea sediments during glacial maxima: Nature Communications, v. 7, doi: 10.1038/ncomms10796.

Chen, X., Romaniello, S.J., Herrmann, A.D., Hardisty, D., Gill, B.C., and Anbar, A.D., 2018, Diagenetic effects on uranium isotope fractionation in carbonate sediments from the Bahamas: Geochimica et Cosmochimica Acta, v. 237, p. 294–311, doi: 10.1016/j.gca.2018.06.026.

Dahl, T.W., Boyle, R.A., Canfield, D.E., Connelly, J.N., Gill, B.C., Lenton, T.M., and Bizzarro, M., 2014, Uranium isotopes distinguish two geochemically distinct stages during the later Cambrian SPICE event: Earth and Planetary Science Letters, v. 401, p. 313–326, doi: 10.1016/j.epsl.2014.05.043.

Davydov, V.I., Korn, D., and Schmitz, M.D., 2012, The Carboniferous Period, inGradstein, F.M., et al., eds., The Geologic Time Scale 2012: Oxford, UK, Elsevier, p. 603–651, https://doi.org /10.1016 /B978-0-44-59425-9.00023-8.

Dunk, R., Mills, R., and Jenkins, W., 2002, A reevaluation of the oceanic uranium budget for the Holocene: Chemical Geology, v. 190, p. 45–67, doi: 10.1016/s0009-2541(02)00110-9.

Elrick, M., Polyak, V., Algeo, T.J., Romaniello, S., Asmerom, Y., Herrmann, A.D., Anbar, A.D., Zhao, L., and Chen, Z.-Q., 2016, Global-ocean redox variation during the middle-late Permian through Early Triassic based on uranium isotope and Th/U trends of marine carbonates: Geology, v. 45, p. 163–166, doi: 10.1130/g38585.1.

Elrick , M., and Read, F.J., 1991, Cyclic Ramp-to-Basin Carbonate Deposits, Lower Mississippian, Wyoming and Montana: A Combined Field and Computer Modeling Study: SEPM Journal of Sedimentary Research, v. Vol. 61, doi: 10.1306/d4267866-2b26-11d7-8648000102c1865d.

Eyles, N., 1993, Earths glacial record and its tectonic setting: Earth-Science Reviews, v. 35, p. 1–248, doi: 10.1016/0012-8252(93)90002-o.

Fielding, C.R., Frank, T.D., Birgenheier, L.P., Rygel, M.C., Jones, A.T., and Roberts, J., 2008, Stratigraphic imprint of the Late Palaeozoic Ice Age in eastern Australia: a record

of alternating glacial and nonglacial climate regime: Journal of the Geological Society, v. 165, p. 129–140.

German Stratigraphic Commission, 2002, Stratigraphic table of Germany 2002: Potsdam, Geoforschungszentrum, Bibliothek.

Ghienne, J.-F., Desrochers, A., Vandenbroucke, T.R., Achab, A., Asselin, E., Dabard, M.-P., Farley, C., Loi, A., Paris, F., Wickson, S., and Veizer, J., 2014, A Cenozoic-style scenario for the end-Ordovician glaciation: Nature Communications, v. 5, doi: 10.1038/ncomms5485.

Giles, K.A., and Dickinson, W.R., 1995, The Interplay of Eustasy and Lithospheric Flexure in Forming Stratigraphic Sequences in Foreland Settings: An Example From The Antler Foreland, Nevada And Utah: Stratigraphic Evolution of Foreland Basins, p. 187–211, doi: 10.2110/pec.95.52.0187.

Giles, K.A., 1996, Giles K A. Tectonically forced retrogradation of the lower Mississippian Joana Limestone, Nevada and Utah: Rocky Mountain Section (SEPM), p. 145–164.

Giles, P.S., 2012, Low-latitude Ordovician to Triassic brachiopod habitat temperatures (BHTs) determined from δ18O[brachiopod calcite]: A cold hard look at ice-house tropical oceans: Palaeogeography, Palaeoclimatology, Palaeoecology, v. 317-318, p. 134–152, doi: 10.1016/j.palaeo.2012.01.002.

Gill, B.C., Lyons, T.W., and Saltzman, M.R., 2007, Parallel, high-resolution carbon and sulfur isotope records of the evolving Paleozoic marine sulfur reservoir: Palaeogeography, Palaeoclimatology, Palaeoecology, v. 256, p. 156–173, doi: 10.1016/j.palaeo.2007.02.030.

Goddéris, Y., Donnadieu, Y., Carretier, S., Aretz, M., Dera, G., Macouin, M., and Regard, V., 2017, Onset and ending of the late Palaeozoic ice age triggered by tectonically paced rock weathering: Nature Geoscience, v. 10, p. 382–386, doi: 10.1038/ngeo2931.

Goebel, K.A., 1991, Interpretation of the lower Mississippian Joana Limestone and implications for the Antler orogenic system [thesis].

González, C.R. New data on the late Palaeozoic glaciations in Argentina: Newsletter on Carboniferous Stratigraphy, v. 19, p. 44–45.

Gulbranson, E.L., Montanez, I.P., Schmitz, M.D., Limarino, C.O., Isbell, J.L., Marenssi, S.A., and Crowley, J.L., 2010, High-precision U-Pb calibration of Carboniferous glaciation and climate history, Paganzo Group, NW Argentina: Geological Society of America Bulletin, v. 122, p. 1480–1498, doi: 10.1130/b30025.1.

Hoogakker, B.A.A., Elderfield, H., Schmiedl, G., Mccave, I.N., and Rickaby, R.E.M., 2014, Glacial–interglacial changes in bottom-water oxygen content on the Portuguese margin: Nature Geoscience, v. 8, p. 40–43, doi: 10.1038/ngeo2317.

Howe, J.N.W., Piotrowski, A.M., Noble, T.L., Mulitza, S., Chiessi, C.M., and Bayon, G., 2016, North Atlantic Deep Water Production during the Last Glacial Maximum: Nature Communications, v. 7, doi: 10.1038/ncomms11765.

Hua, B., Xu, H., Terry, J., and Deng, B., 2006, Kinetics of Uranium(VI) Reduction by Hydrogen Sulfide in Anoxic Aqueous Systems: Environmental Science & Technology, v. 40, p. 4666–4671, doi: 10.1021/es051804n.

Ingall, E., 2005, Sediment carbon, nitrogen and phosphorus cycling in an anoxic fjord, Effingham Inlet, British Columbia: American Journal of Science, v. 305, p. 240–258, doi: 10.2475/ajs.305.3.240.

Ingall, E.D., Bustin, R., and Cappellen, P.V., 1993, Influence of water column anoxia on the burial and preservation of carbon and phosphorus in marine shales: Geochimica et Cosmochimica Acta, v. 57, p. 303–316, doi: 10.1016/0016-7037(93)90433-w.

Isaacson, P., Díaz-Martínez, E., Grader, G., Kalvoda, J., Babek, O., and Devuyst, F., 2008, Late Devonian–earliest Mississippian glaciation in Gondwanaland and its biogeographic consequences: Palaeogeography, Palaeoclimatology, Palaeoecology, v. 268, p. 126–142, doi: 10.1016/j.palaeo.2008.03.047.

Isbell, J.L., Miller, M.F., Wolfe, K.L., and Lenaker, P.A., 2003, Timing of late Paleozoic glaciation in Gondwana: Was glaciation responsible for the development of Northern Hemisphere cyclothems?: Special Paper 370: Extreme depositional environments: mega end members in geologic time, p. 5–24, doi: 10.1130/0-8137-2370-1.5.

Isbell, J.L., Henry, L.C., Gulbranson, E.L., Limarino, C.O., Fraiser, M.L., Koch, Z.J., Ciccioli, P.L., and Dineen, A.A., 2012, Glacial paradoxes during the late Paleozoic ice age: Evaluating the equilibrium line altitude as a control on glaciation: Gondwana Research, v. 22, p. 1–19, doi: 10.1016/j.gr.2011.11.005.

James, N.P., Kendall, A.C., Pufahl, P.K., and Dalrymple, R.M. Introduction to biological and chemical sedimentary facies models. In Facies Models: v. 4, p. 232-339.

Joachimski, M.M., and Buggisch, W., 1993, Anoxic events in the late Frasnian—Causes of the Frasnian-Famennian faunal crisis?: Geology, v. 21, p. 675, doi: 10.1130/0091-7613(1993)021<0675:aeitlf>2.3.co;2.

Johnson, J.G., Klapper, G., and Sandberg, C.A., 1985, Devonian eustatic fluctuations in Euramerica: Geological Society of America Bulletin, v. 96, p. 567, doi: 10.1130/0016-7606(1985)96<567:defie>2.0.co;2.

Kammer, T.W., and Matchen, D.L., 2008, Evidence for eustasy at the Kinderhookian-Osagean (Mississippian) boundary in the United States: Response to late Tournaisian glaciation: Special Paper 441: Resolving the Late Paleozoic Ice Age in Time and Space, p. 261–274, doi: 10.1130/2008.2441(18).

Katz, D.A., Buoniconti, M.R., Montañez, I.P., Swart, P.K., Eberli, G.P., and Smith, L.B., 2007, Timing and local perturbations to the carbon pool in the lower Mississippian Madison Limestone, Montana and Wyoming: Palaeogeography, Palaeoclimatology, Palaeoecology, v. 256, p. 231–253, doi: 10.1016/j.palaeo.2007.02.048.

Klinkhammer, G., and Palmer, M., 1991, Uranium in the oceans: Where it goes and why: Geochimica et Cosmochimica Acta, v. 55, p. 1799–1806, doi: 10.1016/0016-7037(91)90024-y.

Knoll, A., 2000, Learning to tell Neoproterozoic time: Precambrian Research, v. 100, p. 3–20, doi: 10.1016/s0301-9268(99)00067-4.

Kump, L.R., Arthur, M.A., Patzkowsky, M.E., Gibbs, M.T., Pinkus, D.S., and Sheehan, P.M., 1999, A weathering hypothesis for glaciation at high atmospheric pCO2 during the Late Ordovician: Palaeogeography, Palaeoclimatology, Palaeoecology, v. 152, p. 173–187, doi: 10.1016/s0031-0182(99)00046-2.

Kump, L.R., and Arthur, M.A., 1999, Interpreting carbon-isotope excursions: carbonates and organic matter: Chemical Geology, v. 161, p. 181–198, doi: 10.1016/s0009-2541(99)00086-8.

Lau, K.V., Maher, K., Altiner, D., Kelley, B.M., Kump, L.R., Lehrmann, D.J., Silva-Tamayo, J.C., Weaver, K.L., Yu, M., and Payne, J.L., 2016, Marine anoxia and delayed Earth system recovery after the end-Permian extinction: Proceedings of the National Academy of Sciences, v. 113, p. 2360–2365, doi: 10.1073/pnas.1515080113.

Limarino, C., Tripaldi, A., Marenssi, S., and Fauqué, L., 2006, Tectonic, sea-level, and climatic controls on Late Paleozoic sedimentation in the western basins of Argentina: Journal of South American Earth Sciences, v. 22, p. 205–226, doi: 10.1016/j.jsames.2006.09.009.

Liu, J., Algeo, T.J., Qie, W., and Saltzman, M.R., 2018, Intensified Oceanic Circulation During Early Carboniferous Cooling Events: Evidence From Carbon And Nitrogen Isotopes: doi: 10.1130/abs/2018am-319617.

Lu, Z., Hoogakker, B.A.A., Hillenbrand, C.-D., Zhou, X., Thomas, E., Gutchess, K.M., Lu, W., Jones, L., and Rickaby, R.E.M., 2016, Oxygen depletion recorded in upper waters of the glacial Southern Ocean: Nature Communications, v. 7, doi: 10.1038/ncomms11146.

Lutgens, F.K., Tarbuck, E.J., and Tasa, D., 2018, Essentials of geology: NY, NY, Pearson, p 269.

Macdonald, F.A., Swanson-Hysell, N.L., Park, Y., Lisiecki, L., and Jagoutz, O., 2019, Arc-continent collisions in the tropics set Earth's climate state: Science, doi: 10.1126/science.aav5300.

Maharjan, D., Jiang, G., Peng, Y., and Henry, R.A., 2018a, Paired carbonate-organic carbon and nitrogen isotope variations in Lower Mississippian strata of the southern Great Basin, western United States: Palaeogeography, Palaeoclimatology, Palaeoecology, v. 490, p. 462–472, doi: 10.1016/j.palaeo.2017.11.026.

Maharjan, D., Jiang, G., Peng, Y., and Nicholl, M.J., 2018b, Sulfur isotope change across the Early Mississippian K–O (Kinderhookian–Osagean) δ13C excursion: Earth and Planetary Science Letters, v. 494, p. 202–215, doi: 10.1016/j.epsl.2018.04.043.

Martin, J.H., 1990, Glacial-interglacial CO2change: The Iron Hypothesis: Paleoceanography, v. 5, p. 1–13, doi: 10.1029/pa005i001p00001.

Mclennan, S.M., 2001, Relationships between the trace element composition of sedimentary rocks and upper continental crust: Geochemistry, Geophysics, Geosystems, v. 2, doi: 10.1029/2000gc000109.

McManus, J., Berelson, W.M., Severmann, S., Poulson, R.L., Hammond, D.E., Klinkhammer, G.P., and Holm, C., 2006, Molybdenum and uranium geochemistry in continental margin sediments: Paleoproxy potential: Geochimica et Cosmochimica Acta, v. 70, p. 4643–4662, doi: 10.1016/j.gca.2006.06.1564.

Melchin, M.J., Mitchell, C.E., Holmden, C., and Storch, P., 2013, Environmental changes in the Late Ordovician-early Silurian: Review and new insights from black shales and nitrogen isotopes: Geological Society of America Bulletin, v. 125, p. 1635–1670, doi: 10.1130/b30812.1.

Meyer, K.M., and Kump, L.R., 2008, Oceanic Euxinia in Earth History: Causes and Consequences: Annual Review of Earth and Planetary Sciences, v. 36, p. 251–288, doi: 10.1146/annurev.earth.36.031207.124256.

Mii, H.-S., Grossman, E.L., and Yancey, T.E., 1999, Carboniferous isotope stratigraphies of North America: Implications for Carboniferous paleoceanography and Mississippian glaciation: Geological Society of America Bulletin, v. 111, p. 960–973, doi: 10.1130/0016-7606(1999)111<0960:cisona>2.3.co;2.

Montoya-Pino, C., Weyer, S., Anbar, A.D., Pross, J., Oschmann, W., Schootbrugge, B.V.D., and Arz, H.W., 2010, Global enhancement of ocean anoxia during Oceanic Anoxic Event 2: A quantitative approach using U isotopes: Geology, v. 38, p. 315–318, doi: 10.1130/g30652.1.

Montañez, I.P., and Poulsen, C.J., 2013, The Late Paleozoic Ice Age: An Evolving Paradigm: Annual Review of Earth and Planetary Sciences, v. 41, p. 629–656.

Morford, J.L., and Emerson, S., 1999, The geochemistry of redox sensitive trace metals in sediments: Geochimica et Cosmochimica Acta, v. 63, p. 1735–1750, doi: 10.1016/s0016-7037(99)00126-x.

Morford, J.L., Martin, W.R., and Carney, C.M., 2009, Uranium diagenesis in sediments underlying bottom waters with high oxygen content: Geochimica et Cosmochimica Acta, v. 73, p. 2920–2937, doi: 10.1016/j.gca.2009.02.014.

New Brunswick Laboratory, 2008, Certificate of Analysis, CRM 145 Uranyl (Normal) Nitrate Assay and Isotopic Solution, Document issued by New Bruswick Laboratory, US Department of Energy.

Pedersen, T.F., 1983, Increased productivity in the eastern equatorial Pacific during the last glacial maximum (19,000 to 14,000 yr B.P): Geology, v. 11, p. 16, doi: 10.1130/0091-7613(1983)11<16:ipitee>2.0.co;2.

Piper, D., and Perkins, R., 2004, A modern vs. Permian black shale—the hydrography, primary productivity, and water-column chemistry of deposition: Chemical Geology, v. 206, p. 177–197, doi: 10.1016/j.chemgeo.2003.12.006.

Poole, F.G., 1974, Flysch Deposits Of Antler Foreland Basin, Western United States: Tectonics and Sedimentation, p. 58–82, doi: 10.2110/pec.74.22.0058.

Qie, W., Zhang, X., Du, Y., and Zhang, Y., 2010, Lower Carboniferous carbon isotope stratigraphy in South China: Implications for the Late Paleozoic glaciation: Science China Earth Sciences, v. 54, p. 84–92, doi: 10.1007/s11430-010-4062-4.

Romaniello, S.J., Herrmann, A.D., and Anbar, A.D., 2013, Uranium concentrations and 238U/235U isotope ratios in modern carbonates from the Bahamas: Assessing a novel paleoredox proxy: Chemical Geology, v. 362, p. 305–316, doi: 10.1016/j.chemgeo.2013.10.002.

Ross, C.A., and Ross, J.R.P., 1987, Biostratigraphic zonation of Late Paleozoic depositional sequences: Cushman Foundation for Foraminiferal Research.

Saltzman, M.R., González, L.A., and Lohmann, K.C., 2000, Earliest Carboniferous cooling step triggered by the Antler orogeny?: Geology, v. 28, p. 347–350, doi: 10.1130/0091-7613(2000)028<0347:eccstb>2.3.co;2.

Saltzman, M.R., 2002, Carbon and oxygen isotope stratigraphy of the Lower Mississippian (Kinderhookian–lower Osagean), western United States: Implications for seawater chemistry and glaciation: Geological Society of America Bulletin, v. 114, p. 96–108, doi: 10.1130/0016-7606(2002)114<0096:caoiso>2.0.co;2.

Saltzman, M.R., 2003, Organic Carbon Burial and Phosphogenesis in the Antler Foreland Basin: An Out-of-Phase Relationship During the Lower Mississippian: Journal of Sedimentary Research, v. 73, p. 844–855, doi: 10.1306/032403730844.

Saltzman, M., Groessens, E., and Zhuravlev, A., 2004, Carbon cycle models based on extreme changes in δ13C: an example from the lower Mississippian: Palaeogeography, Palaeoclimatology, Palaeoecology, v. 213, p. 359–377, doi: 10.1016/s0031-0182(04)00389-x.

Saltzman, M.R., 2005, Phosphorus, nitrogen, and the redox evolution of the Paleozoic oceans: Geology, v. 33, p. 573, doi: 10.1130/g21535.1.

Schauble, E.A., 2007, Role of nuclear volume in driving equilibrium stable isotope fractionation of mercury, thallium, and other very heavy elements: Geochimica et Cosmochimica Acta, v. 71, p. 2170–2189, doi: 10.1016/j.gca.2007.02.004.

Scholle, P.A., and Arthur, M.A., 1980, Carbon Isotope Fluctuations in Cretaceous Pelagic Limestones: Potential Stratigraphic and Petroleum Exploration Tool: AAPG Bulletin, v. 64, doi: 10.1306/2f91892d-16ce-11d7-8645000102c1865d.

Singler, C.S., 1987, Carbonate petrology and conodont biostratigraphy of a Mississippian carbonate unit, East Pahranagat Range, Lincoln County, Nevada [thesis].

Smith, L.B., and Read, J.F., 2000, Rapid onset of late Paleozoic glaciation on Gondwana: Evidence from Upper Mississippian strata of the Midcontinent, United States: Geology, v. 28, p. 279–282, doi: 10.1130/0091-7613(2000)028<0279:roolpg>2.3.co;2.

Song, H., Song, H., Algeo, T.J., Tong, J., Romaniello, S.J., Zhu, Y., Chu, D., Gong, Y., and Anbar, A.D., 2017, Uranium and carbon isotopes document global-ocean redox-productivity relationships linked to cooling during the Frasnian-Famennian mass extinction: Geology, v. 45, p. 887–890, doi: 10.1130/g39393.1.

Spötl, C., and Vennemann, T.W., 2003, Continuous-flow isotope ratio mass spectrometric analysis of carbonate minerals: Rapid Communications in Mass Spectrometry, v. 17, p. 1004–1006, doi: 10.1002/rcm.1010.

Stal, L.J., 2009, Is the distribution of nitrogen-fixing cyanobacteria in the oceans related to temperature?: Environmental Microbiology, v. 11, p. 1632–1645, doi: 10.1111/j.1758-2229.2009.00016.x.

Stein, R., 1986, Organic carbon and sedimentation rate — Further evidence for anoxic deep-water conditions in the Cenomanian/Turonian Atlantic Ocean: Marine Geology, v. 72, p. 199–209, doi: 10.1016/0025-3227(86)90119-2.

Stewart, J.H., and Poole, F.G., 1974, Lower Paleozoic And Uppermost Precambrian Cordilleran Miogeocline, Great Basin, Western United States: Tectonics and Sedimentation, p. 28–57.

“The World Ocean.” The Columbia Encyclopedia. CD-ROM. 2007, 6th Ed. New York: Columbia University Press.

Tissot, F.L., and Dauphas, N., 2015, Uranium isotopic compositions of the crust and ocean: Age corrections, U budget and global extent of modern anoxia: Geochimica et Cosmochimica Acta, v. 167, p. 113–143, doi: 10.1016/j.gca.2015.06.034.

Tribovillard, N., Algeo, T.J., Lyons, T., and Riboulleau, A., 2006, Trace metals as paleoredox and paleoproductivity proxies: An update: Chemical Geology, v. 232, p. 12–32, doi: 10.1016/j.chemgeo.2006.02.012.

Veevers, J.J., and Powell, C.M., 1987, Late Paleozoic glacial episodes in Gondwanaland reflected in transgressive-regressive depositional sequences in Euramerica: Geological

Society of America Bulletin, v. 98, p. 475, doi: 10.1130/0016-7606(1987)98<475:lpgeig>2.0.co;2.

Veizer, J., Ala, D., Azmy, K., Bruckschen, P., Buhl, D., Bruhn, F., Carden, G.A., Diener, A., Ebneth, S., Godderis, Y., Jasper, T., Korte, C., Pawellek, F., Podlaha, O.G., et al., 1999, 87Sr/86Sr, δ13C and δ18O evolution of Phanerozoic seawater: Chemical Geology, v. 161, p. 59–88, doi: 10.1016/s0009-2541(99)00081-9.

Verbruggen, A., Alonso, A., Eykens, R., Kehoe, F., Kuhn, H., Richter, S., and Aregbe, Y., 2008, Preparation and certification of IRMM-3636, IRMM-3636a and IRMM-3636b: JRC Scientific and Technical Reports, doi: 10.2787/60083.

Walker, L.J., Wilkinson, B.H., and Ivany, L.C., 2002, Continental Drift and Phanerozoic Carbonate Accumulation in Shallow-Shelf and Deep-Marine Settings: The Journal of Geology, v. 110, p. 75-87, doi: 10.1086/324318.

Wallace, Z.A., and Elrick, M., 2014, Early Mississippian Orbital-Scale Glacio-Eustasy Detected From High-Resolution Oxygen Isotopes of Marine Apatite (Conodonts): Journal of Sedimentary Research, v. 84, p. 816–824, doi: 10.2110/jsr.2014.69.

Waters, C.N., and Condon, D.J., 2012, Nature and timing of Late Mississippian to Mid-Pennsylvanian glacio-eustatic sea-level changes of the Pennine Basin, UK: Journal of the Geological Society, v. 169, p. 37–51, doi: 10.1144/0016-76492011-047.

Weyer, S., Anbar, A., Gerdes, A., Gordon, G., Algeo, T., and Boyle, E., 2008, Natural fractionation of 238U/235U: Geochimica et Cosmochimica Acta, v. 72, p. 345–359, doi: 10.1016/j.gca.2007.11.012.

White, D.A., Elrick, M., Romaniello, S., and Zhang, F., 2018, Global seawater redox trends during the Late Devonian mass extinction detected using U isotopes of marine limestones: Earth and Planetary Science Letters, v. 503, p. 68–77, doi: 10.1016/j.epsl.2018.09.020.

Yao, L., Qie, W., Luo, G., Liu, J., Algeo, T.J., Bai, X., Yang, B., and Wang, X., 2015, The TICE event: Perturbation of carbon–nitrogen cycles during the mid-Tournaisian (Early Carboniferous) greenhouse–icehouse transition: Chemical Geology, v. 401, p. 1–14, doi: 10.1016/j.chemgeo.2015.02.021.

Zhang, F., Algeo, T.J., Romaniello, S.J., Cui, Y., Zhao, L., Chen, Z.-Q., and Anbar, A.D., 2018a, Congruent Permian-Triassic δ238U records at Panthalassic and Tethyan sites: Confirmation of global-oceanic anoxia and validation of the U-isotope paleoredox proxy: Geology, v. 46, p. 327–330, doi: 10.1130/g39695.1.

Zhang, F., Romaniello, S.J., Algeo, T.J., Lau, K.V., Clapham, M.E., Richoz, S., Herrmann, A.D., Smith, H., Horacek, M., and Anbar, A.D., 2018b, Multiple episodes of extensive marine anoxia linked to global warming and continental weathering following the latest Permian mass extinction: Science Advances, v. 4, doi: 10.1126/sciadv.1602921.

Zheng, Y., Anderson, R.F., Geen, A.V., and Kuwabara, J., 2000, Authigenic molybdenum formation in marine sediments: a link to pore water sulfide in the Santa Barbara Basin: Geochimica et Cosmochimica Acta, v. 64, p. 4165–4178, doi: 10.1016/s0016-7037(00)00495-6.

Zheng, Y., Anderson, R.F., Geen, A.V., and Fleisher, M.Q., 2002, Preservation of particulate non-lithogenic uranium in marine sediments: Geochimica et Cosmochimica Acta, v. 66, p. 3085–3092, doi: 10.1016/s0016-7037(01)00632-9.

Zhou, C., Xiao, S., Wang, W., Guan, C., Ouyang, Q., and Chen, Z., 2017, The stratigraphic complexity of the middle Ediacaran carbon isotopic record in the Yangtze Gorges area, South China, and its implications for the age and chemostratigraphic significance of the Shuram excursion: Precambrian Research, v. 288, p. 23–38, doi: 10.1016/j.precamres.2016.11.007.

Figures

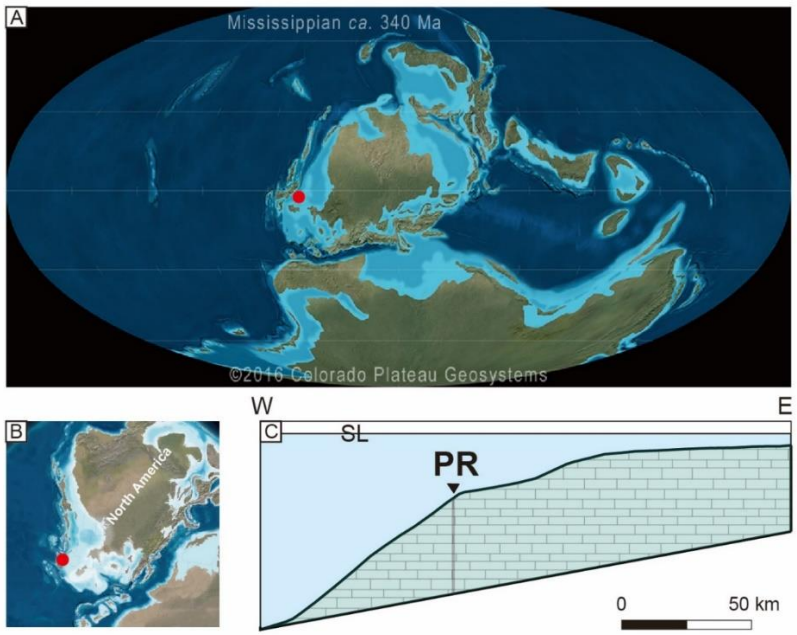

Figure 1. (A) Early Mississippian paleogeographic map from Blakey, (2016). (B) Early Mississippian paleogeography of North American from Blakey, (2013). (C) Schematic east-west cross section across the Early-Middle Mississippian carbonate ramp showing location of study area (labelled PR) along the outer to middle carbonate ramp (modified from Giles, 1996; Maharjan et al., 2018b). Carbonate ramp deposits are overlain by the Middle Mississippian Chainman Shale. Red circle indicates location of study area in southern Nevada. Red circle indicates location of study area in southern Nevada.

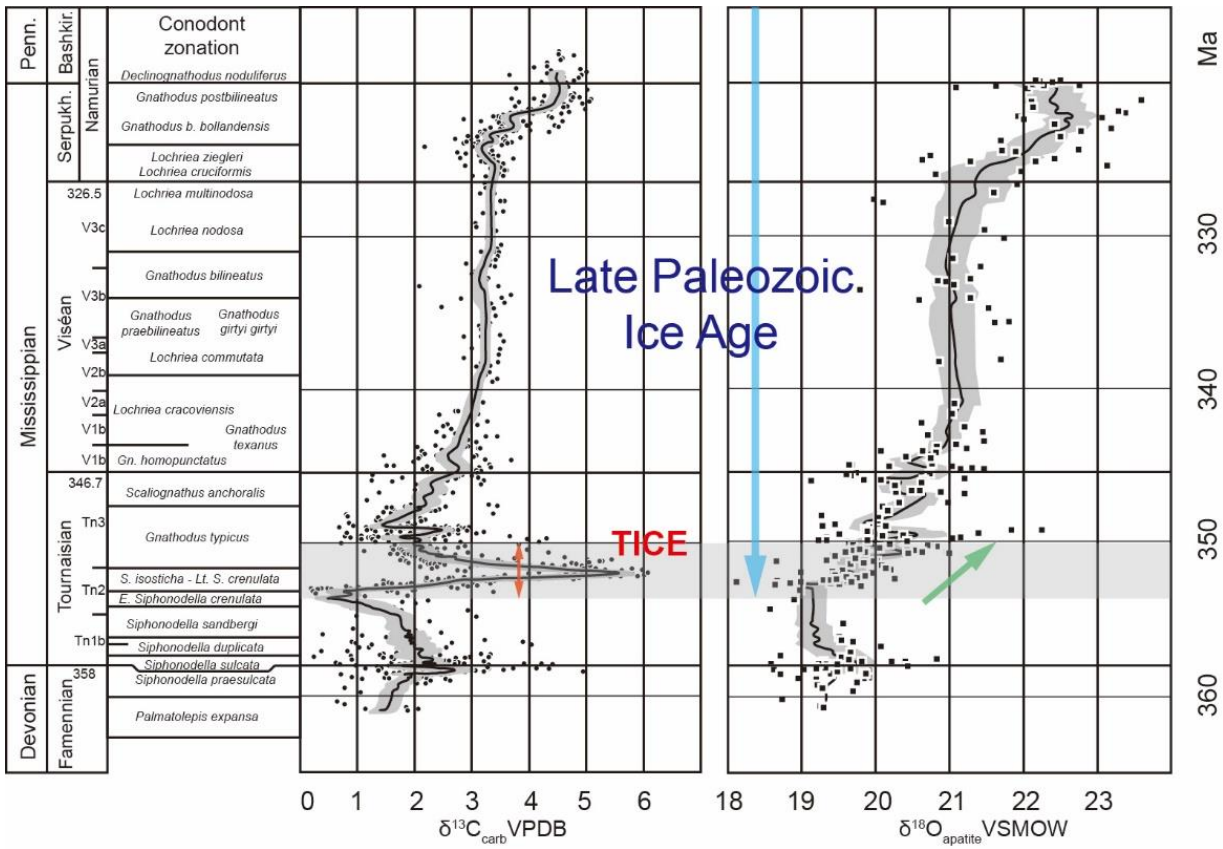

Figure 2. Carbon and oxygen isotope (from conodont apatite) variations from the Late Devonian to Late Mississippian (modified from Buggisch et al., 2008). The prominent Tournaisian positive carbon isotope excursion (TICE) is outlined with red arrow. Note that the positive $\delta^{18}O$ shift begins simultaneously with the TICE onset (green arrow) suggesting cooling associated with the burial of organic matter. Blue arrow outlines the Mississippian portion of the late Paleozoic ice age (LPIA).

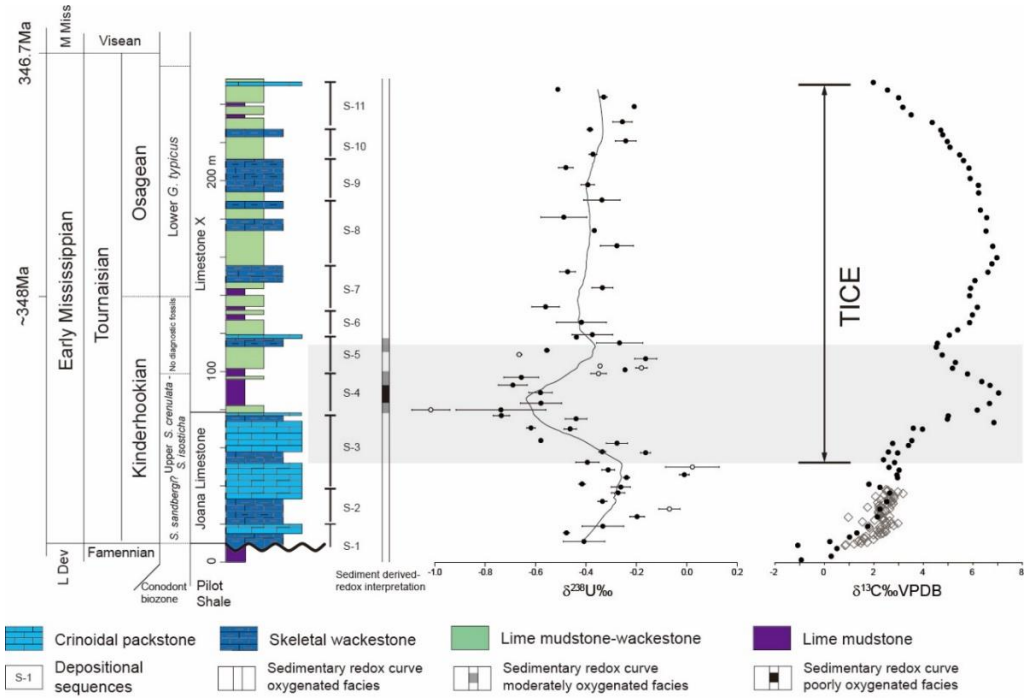

Figure 3. Stratigraphy, conodont biostratigraphy, sequence stratigraphy, depositional redox interpretations, and U and C isotope stratigraphy of the studied section. Gray shading outlines extent of anoxic event termed the Tournaisian ocean anoxic event (TOAE) defined by the negative U isotope excursion. Open circles in U isotope curve are interpreted as outliers. Gray open diamonds in C isotope curve come from published C-isotope values of Maharjan et al. (2018a) from the same Pahranaghat Range location and are added to the curve (filled black circles) to better define the onset timing of the Tournaisian positive carbon isotope excursion (TICE). Conodont zone age control from Maharjan et al. (2018a).

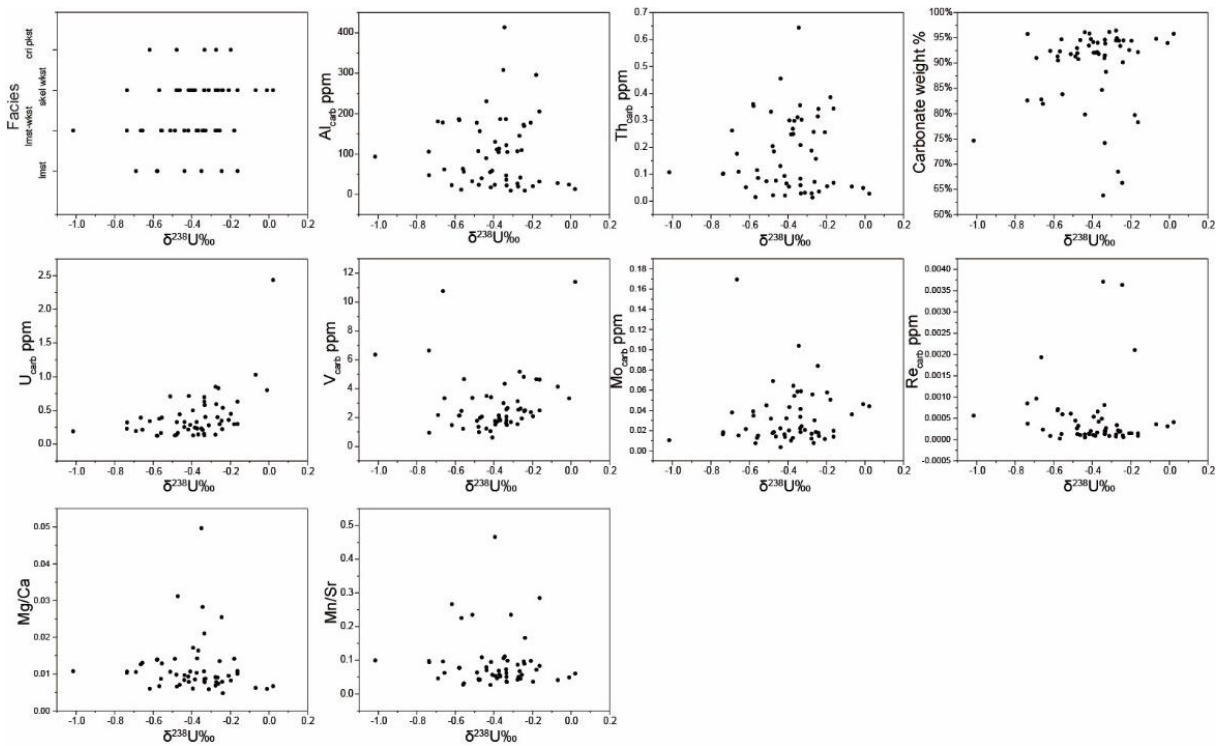

Figure 4. Cross plots of $\delta^{238}U$ against facies, detrital sediment proxies (Al, Th, carb wt%), redox proxies (U, V, Mo, Re, Mn/Sr), and dolomitization (Mg/Ca, Mn/Sr). Note the lack of co-variation among the various geochemical proxies indicating the measured $\delta^{238}U$ values were not influenced by local processes. Lmst = Lime mudstone, lmst-wkst = Lime mudstone-wackestone, skel wkst = skeletal wackestone, cri pkst = crinoidal packstone.

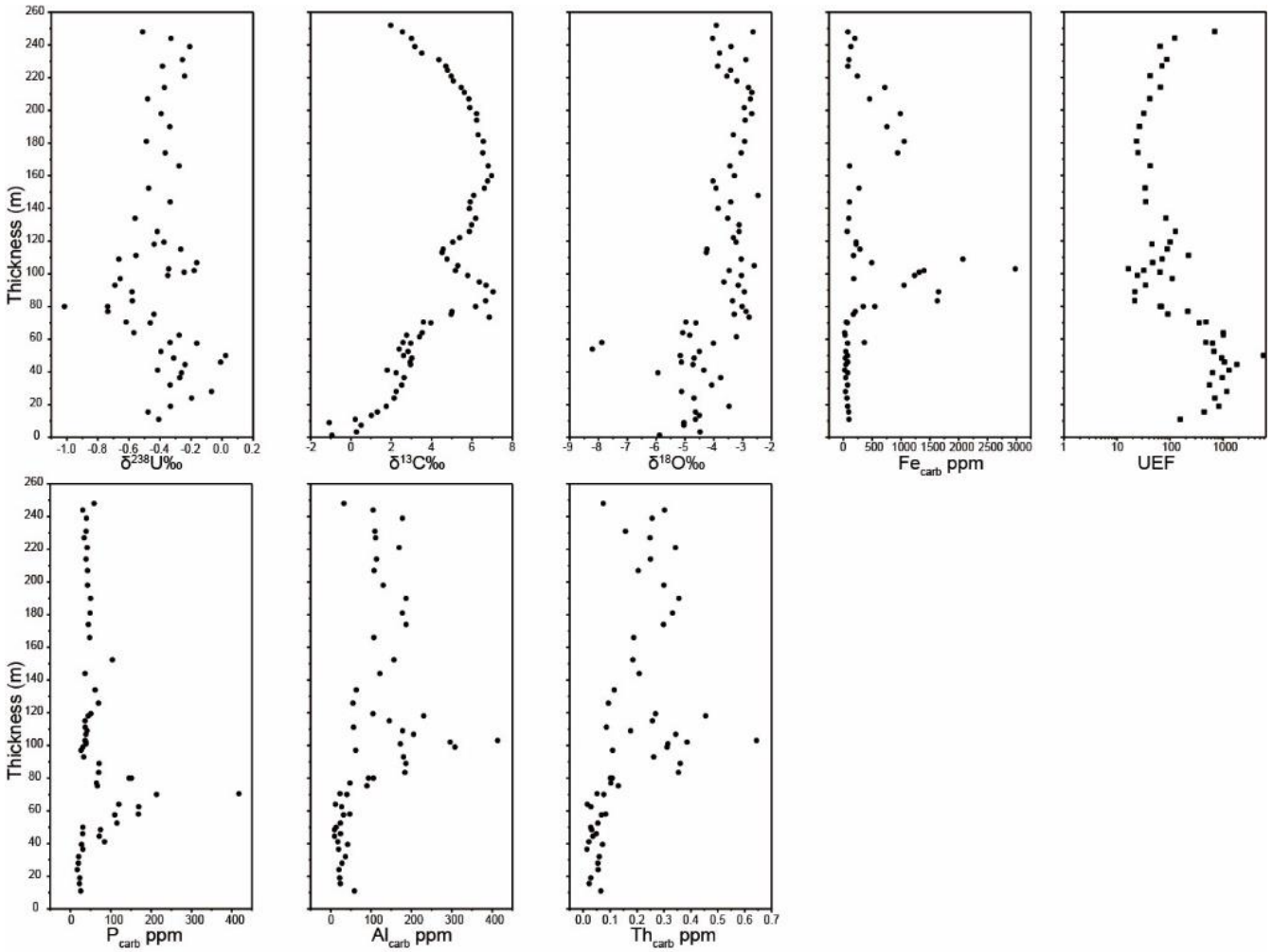

Figure 5. U, C, and O isotope stratigraphy of studied section to compare to measured elemental and U enrichment factor (UEF).

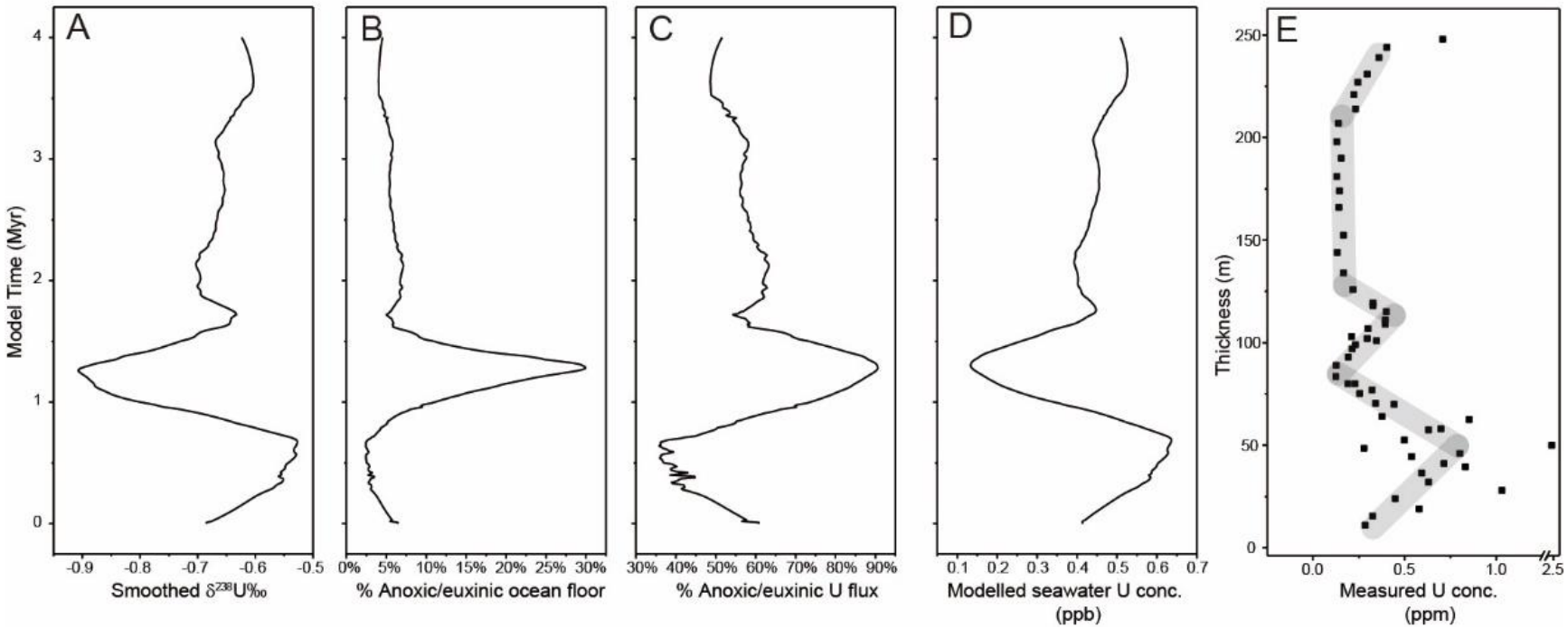

Figure 6. Results from dynamic uranium model. (A) LOWESS-smoothed $\delta^{238}U$ curve. (B) Modeled changes in percent euxinic/anoxic seafloor. (C) Modeled changes in percent seawater U into euxinic/anoxic sediments. (D) Modeled changes in concentration of seawater U. (E) Changes in uranium concentrations measured in carbonate fraction. See text for explanations of differences between modeled and measured U relative concentrations.

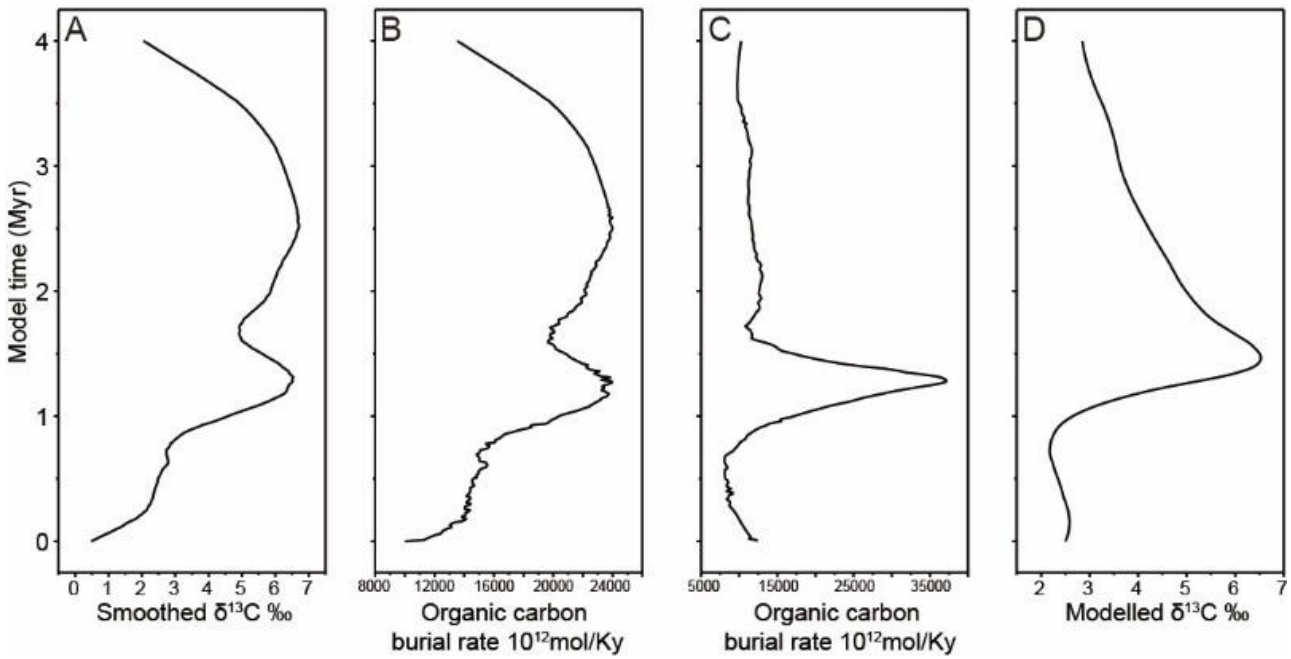

Figure 7. (A) LOWESS-smoothed $\delta^{13}C$ curve. (B) Modeled variations in organic carbon burial rate estimated from the smoothed $\delta^{13}C$ curve. (C) Modeled variations in organic carbon burial rate estimated from changes in modeled euxinic/anoxic ocean floor percentages from Figure 6B. (D) Modeled $\delta^{13}C$ curve generated using organic carbon burial changes shown in Figure 7C.

Tables

Table 1. Facies description and depositional environment interpretation of Joana Limestone and Limestone X at Pahranagat Range section.

Facies	Lime-mudstone	Lime-mudstone-wackestone	Skeletal wackestone	Skeletal wackestone-packstone	Packstone
Lithology	Dark gray, lime mudstone	Dark gray-gray, skeletal lime-mudstone-wackestone	Dark gray, skeletal wackestone, sparse chert nodules/layers	Medium gray, skeletal wackestone-packstone	Gray-light gray, uneven bedded, skeletal packstone
Sedimentary strucrures	Medium to thin bedded, suspension laminations, graded beds	Medium to thin bedded, nodular bedding, graded beds, lenticular beds, sparse suspension laminations	Medium to thin bedded, nodular bedding, graded beds	Medium to thick bedded, nodular bedding	Uneven beddings, med-thick beddings
Skeletal/trace fossil	Sparse crinoids, brachiopods, tabulate corals; sparse bioturbation	Whole or broken crinoids, brachiopods, rugose corals;	Whole or broken rugose corals, brachiopods, crinoids,	Whole or broken tabulate corals, rugose	Whole or broken brachiopods, rugose corals, crinoids and

	including Zoophycus and Chondrites	bioturbation including sparse Zoophycus	gastropods bioturbation	corals, brachiopods; bioturbation	skeleton fragments; General bioturbated
Depositional environment and oxygenation interpretation	poorly oxygenated, offshore to lower shoreface, outer ramp	moderately oxygenated, lower shoreface, middle to outer ramp	Middle ramp add other things	Middle-inner ramp add other things	Inner ramp

Table 2. Dynamic uranium model parameters.

Parameter	Value	Reference
$\delta^{238}U_{river}$	-0.29‰	
J_{river}	4.20×10^{16} nmol/yr	Morford and Emerson, 1999
k_{oxic}	28 nmol/m2·yr·nMU	Dunk et al.,2002
k_{anox}	629 nmol/m2·yr·nMU	Zheng et al.,2000, 2002; McManus et al.,2006
Δ_{oxic}	0‰	White et al., 2018
Δ_{anox}	0.65‰	White et al., 2018
Ao	3.62×10^{14} m^2	Lutgens, Frederick. Essentials of Geology. New York: MacMillan, 1992: 269.
Vo	1.34×10^{21} L	"The World Ocean." The Columbia Encyclopedia. CD-ROM. 2007, 6th Ed. New York: Columbia University Press
$\delta^{238}U_{initial}$	-0.68	First value of $\delta^{238}U$ curve
U conc $_{initial}$	1.74×10^{-9}	Calculated from steady state
Fanox $_{initial}$	6%	Calculated from steady state

Table 3. Carbon burial model parameters.

Parameter	Value	Reference
F_w	56000×10^{12} mol/Kyr	Kump and Arthur, 1999
F_{bcarb}	40000×10^{12} mol/Kyr	Kump and Arthur, 1999
F_{borg}	10000×10^{12} mol/Kyr	Kump and Arthur, 1999
$\delta^{13}C_w$	-3.97‰	Calculated from steady state
Δ_{org}	-25‰	Kump and Arthur, 1999
Δ_{carb}	0‰	Calculated from steady state
$\delta^{13}C_{initial}$	0.49‰	From measurement
Anoxic OC burial	307.29 mol/m2/Ky	Berner, 1982
Oxic OC burial	15.16	Calculated from Early Mississippian background fanox
Background fanox	4%	Average of pre&post-TOAE $\delta^{238}U$ values

Table 4. Data of $\delta^{238}U$, $\delta^{13}C$, $\delta^{18}O$, elemental concentrations and lithology of samples.

Sample	Meters	lithology	$\delta^{13}C$	$\delta^{18}O$	$\delta^{238}U$	2sd	Mg	Al	P	Ca	V	Mn	Fe	Sr	Mo	Re	Th	U
	m		‰	‰	‰		(ppm)	(ppm)	(ppm)	(ppm)	(ppm)	(ppm)	(ppm)	(ppm)	(ppm)	(ppm)	(ppm)	(ppm)
PR1.4	1.4	wackestone	-0.94	-5.89														
PR3.3	3.3	mudstone																
PR7.4	7.4	wackestone	0.51	-5.04														
PR9	9	wackestone	-1.08	-5.04														
PR11	11	wackestone	0.22	-4.64	-0.41	0.16	3989.84	58.66	25.78	373840.07	0.62	21.39	97.57	374.92	0.03	0.00020	0.07	0.28
PR13.4	13.4	packstone																
PR15.5	15.5	packstone	1.31	-4.64	-0.48	0.02	2408.42	23.75	22.43	364809.02	1.00	12.50	93.11	301.52	0.07	0.00013	0.02	0.33
PR17.5	17.5	packstone																
PR19	19	packstone	1.75	-3.48	-0.33	0.16	2895.09	22.26	23.31	371871.69	1.48	11.41	74.09	323.55	0.06	0.00020	0.03	0.58
PR21.2	21.2	wackestone																
PR24	24	packstone	2.14	-4.69	-0.20	0.06	3076.65	20.50	17.21	373841.05	2.09	12.30	61.67	338.44	0.06	0.00015	0.06	0.45
PR26	26	wackestone																
PR28	28	wackestone	2.24	-5.12	-0.07	0.08	2346.26	28.10	19.75	376318.61	4.14	14.66	37.39	354.33	0.04	0.00036	0.05	1.03
PR30.6	30.6	wackestone																
PR32	32	wackestone	2.52	-4.08	-0.33	0.04	3204.08	36.46	20.48	374359.89	2.07	17.25	72.32	339.14	0.04	0.00020	0.06	0.63
PR34.3	34.3	packstone																
PR36.5	36.5	packstone	2.64	-3.77	-0.27	0.05	2946.92	19.65	30.93	376041.75	2.54	20.40	40.45	406.07	0.06	0.00034	0.01	0.59
PR37.8	37.8	wackestone-packstone																
PR39.5	39.5	wackestone-packstone	2.24	-5.94			2760.20	41.92	27.68	374310.22	2.63	14.96	75.52	331.23	0.03	0.00019	0.07	0.83
PR41.1	41.1	wackestone-packstone																
PRX0.6	41.1	wackestone-packstone			-0.42	0.02	2984.54	17.57	84.63	379558.02	3.41	72.89	23.56	768.82	0.01	0.00013	0.02	0.71
PR42	42	wackestone-packstone																
PR42.5	42.5	wackestone-packstone																
PRX2	42.5	wackestone-packstone																
PR44	44	wackestone-packstone																

PR44.5	44.5	wackestone-packstone																
PRX4	44.5	wackestone-packstone	2.96	-4.72	-0.24	0.02	1798.62	9.48	71.56	375807.43	2.50	65.77	43.12	394.52	0.01	0.00006	0.04	0.54
PR46	46	wackestone-packstone	2.93	-5.13	-0.01	0.04	2221.40	24.24	30.52	373191.33	3.33	15.93	76.70	323.89	0.05	0.00031	0.05	0.80
PR46.5	46.5	wackestone-packstone																
PRX6	46.5	wackestone-packstone																
PR48	48	wackestone-packstone																
PR48.5	48.5	wackestone-packstone																
PRX8	48.5	wackestone-packstone	3.02	-4.69	-0.31	0.05	2241.67	9.42	74.72	381914.18	1.69	72.49	33.02	308.33	0.02	0.00009	0.03	0.28
PR50	50	wackestone-packstone	2.61	-5.17			2548.48	13.52	30.86	379981.65	11.40	20.85	72.40	344.41	0.04	0.00041	0.03	2.44
PR50.5	50.5	wackestone-packstone																
PRX10	50.5	wackestone-packstone																
PR51.5	51.5	wackestone-packstone																
PR52.5	52.5	wackestone-packstone																
PRX12	52.5	wackestone-packstone	2.83	-4.50	-0.39	0.09	2251.86	23.85	115.30	373867.19	1.77	133.79	43.65	287.16	0.02	0.00011	0.05	0.50
PR54	54	wackestone-packstone	2.39	-8.21														
PR55	55	wackestone-packstone																
PRX14.5	55	wackestone-packstone																
PR55.5	55.5	wackestone-packstone																
PR57.5	57.5	wackestone																
PRX17	57.5	wackestone	2.96	-4.01	-0.16	0.04	3930.94	31.83	110.04	363609.38	2.49	112.64	72.80	395.65	0.02	0.00009	0.07	0.63
PR58	58	wackestone	2.58	-7.89	-0.34	0.03	2343.68	47.27	168.55	293766.61	2.57	29.01	364.17	466.00	0.03	0.00014	0.08	0.70
PR59.4	59.4	wackestone																
PRX18.9	59.4	wackestone																
PR60	60	wackestone																
PR61.5	61.5	wackestone																
PRX21	61.5	wackestone	3.40	-3.22														
PR62.5	62.5	wackestone	2.76	-4.84	-0.28	0.08	2627.04	27.00	169.43	382454.68	3.13	53.06	30.74	611.94	0.02	0.00012	0.03	0.85
PR64	64	wackestone																
PR64	64	wackestone-packstone																
PRX23.5	64	wackestone-packstone	3.53	-5.08	-0.58	0.01	2451.13	11.96	120.12	366251.65	2.46	67.27	21.87	298.40	0.01	0.00002	0.02	0.38

PR66	66	wackestone																
PR66	66	wackestone-packstone																
PRX25.5	66	wackestone-packstone																
PR68	68	wackestone																
PR68.5	68.5	wackestone-packstone																
PRX28	68.5	wackestone-packstone																
PR70	70	wackestone	3.96	-4.62	-0.46	0.05	2641.73	40.15	213.47	374947.43	2.06	53.23	66.89	488.98	0.01	0.00011	0.08	0.44
PR70.5	70.5	packstone-grainstone																
PRX30	70.5	packstone-grainstone	3.59	-4.97	-0.62	0.03	2200.75	23.05	417.43	366928.85	1.48	98.01	52.16	367.77	0.02	0.00009	0.05	0.34
PR72	72	packstone																
PR72	72	packstone																
PRX31.5	72	packstone																
PR73.5	73.5	packstone																
PR73.5	73.5	mudstone-wackestone																
PRX33	73.5	mudstone-wackestone	6.85	-2.78														
PR75.3	75.3	mudstone-wackestone	4.97	-3.29	-0.44	0.09	3188.57	89.80	66.97	380409.24	1.24	44.44	174.32	559.43	0.02	0.00012	0.13	0.25
PR75.5	75.5	mudstone-wackestone																
PRX35	75.5	mudstone-wackestone																
PR77	77	wackestone-packstone																
PR77	77	wackestone-packstone																
PRX36.5	77	wackestone-packstone	5.01	-2.88	-0.74	0.06	4025.17	47.67	64.48	377871.63	0.95	37.52	207.62	397.53	0.02	0.00037	0.10	0.32
PR78	78	packstone																
PR80	80	mudstone-wackestone	6.18	-3.02	-0.74	0.36	3365.30	105.99	145.50	326086.01	6.64	70.25	545.74	717.57	0.02	0.00085	0.10	0.23
PR81.8	81.8	mudstone-wackestone																
PR83.5	83.5	mudstone	6.68	-3.35	-0.58	0.16	4953.23	183.88	70.00	355654.50	2.14	63.31	1629.56	820.65	0.03	0.00072	0.35	0.12
PR85.5	85.5	mudstone																
PR87	87	mudstone																
PR89	89	mudstone	7.04	-2.94	-0.58	0.09	4977.98	186.13	71.17	358668.05	2.14	63.76	1650.21	824.05	0.04	0.00068	0.36	0.13
PR91	91	mudstone																
PR93	93	mudstone	6.69	-3.16	-0.69	0.11	3790.37	180.50	33.04	359206.96	2.18	38.78	1051.97	840.57	0.04	0.00096	0.26	0.19

PR95	95	mudstone	6.36	-3.65														
PR97	97	mudstone-wackestone			-0.66	0.14	4204.85	62.13	26.54	322305.68	3.34	31.49	180.88	503.71	0.02	0.00024	0.11	0.21
PR99	99	mudstone	5.79	-3.04	-0.35	0.06	15757.74	307.87	30.92	317163.94	3.00	54.16	1234.83	509.63	0.06	0.00049	0.31	0.23
PR101	101	mudstone			-0.24	0.01	6528.56	172.63	38.77	256376.21	4.82	51.50	1315.00	532.70	0.08	0.00363	0.31	0.35
PR102	102	mudstone-wackestone	5.18	-3.47	-0.18	0.05	4430.30	295.89	38.78	313030.01	4.65	52.43	1398.75	729.38	0.05	0.00210	0.39	0.30
PR103	103	mudstone-wackestone			-0.34	0.00	6946.33	413.37	36.44	245865.83	4.35	64.69	2981.30	582.17	0.10	0.00371	0.64	0.21
PR105	105	mudstone-wackestone	5.30	-2.60														
PR106.8	106.8	mudstone			-0.16	0.09	3112.87	205.34	38.44	309128.99	4.63	60.34	490.98	723.24	0.01	0.00015	0.34	0.30
PR109	109	mudstone-wackestone	4.76	-3.05	-0.66	0.02	4116.14	178.00	41.33	325810.59	10.76	61.06	2072.98	632.93	0.17	0.00193	0.18	0.39
PR111.2	111.2	mudstone-wackestone					4252.01	56.62	36.74	329777.17	4.66	34.50	176.59	1094.91	0.02	0.00060	0.09	0.39
PR113.1	113.1	mudstone-wackestone	4.52	-4.26														
PR115.1	115.1	mudstone-wackestone	4.57	-4.24			2454.91	145.19	36.29	270901.26	5.18	36.93	288.76	546.46	0.01	0.00022	0.26	0.40
PR118.1	118.1	mudstone					3061.39	230.50	44.19	315370.52	3.50	38.07	221.57	540.84	0.00	0.00005	0.46	0.33
PR119.4	119.4	mudstone-wackestone	5.05	-3.23	-0.37	0.16	3756.61	104.84	50.88	363844.00	2.15	35.74	222.00	518.90	0.01	0.00017	0.27	0.33
PR122.1	122.1	mudstone-wackestone	5.39	-3.32														
PR124	124	mudstone-wackestone																
PR125.9	125.9	mudstone-wackestone	5.87	-3.13	-0.42	0.20	3437.95	55.27	69.85	369460.39	1.06	21.79	65.93	816.03	0.02	0.00014	0.09	0.22
PR128.2	128.2	mudstone																
PR130	130	mudstone	5.98	-3.13														
PR132	132	mudstone-wackestone																
PR134	134	mudstone-wackestone	6.18	-3.52	-0.56	0.11	3255.65	63.45	61.32	374647.90	1.23	21.21	95.67	768.19	0.01	0.00013	0.12	0.16
PR136	136	mudstone-wackestone																
PR138	138	mudstone-wackestone																
PR140	140	mudstone-wackestone	5.87	-3.86														
PR141.8	141.8	mudstone-wackestone																
PR144	144	mudstone-wackestone	5.91	-3.42	-0.33	0.08	7481.79	121.81	36.38	356083.43	1.81	25.70	105.61	682.25	0.02	0.00013	0.21	0.13
PR146	146	mudstone-wackestone																
PR148	148	wackestone-packstone	6.09	-2.47														
PR149.9	149.9	wackestone-packstone																
PR152.4	152.4	wackestone-packstone	6.61	-3.93			10852.31	156.68	104.05	348392.67	1.98	28.13	271.08	659.89	0.02	0.00032	0.18	0.16

PR154	154	wackestone-packstone																
PR156.8	156.8	mudstone	6.77	-4.03														
PR158	158	mudstone																
PR160	160	mudstone	6.97	-3.29														
PR162	162	mudstone																
PR164	164	mudstone-wackestone																
PR166	166	mudstone-wackestone	6.80	-3.44	-0.28	0.13	3416.95	106.94	47.88	373610.88	1.54	31.63	108.48	746.84	0.01	0.00007	0.19	0.14
PR167.5	167.5	mudstone-wackestone																
PR172	172	mudstone-wackestone																
PR174	174	mudstone-wackestone	6.54	-3.05	-0.37	0.00	5887.20	186.52	44.52	359459.98	1.81	38.26	941.45	729.63	0.05	0.00042	0.30	0.14
PR176.6	176.6																	
PR179	179	wackestone																
PR181	181	mudstone-wackestone	6.56	-2.93	-0.49	0.18	5065.48	177.37	48.93	358588.29	1.78	43.60	1054.76	684.17	0.03	0.00045	0.33	0.13
PR183	183	mudstone-wackestone																
PR185	185	wackestone	6.31	-3.32														
PR187.2	187.2	wackestone																
PR190	190	wackestone			-0.34	0.14	3850.93	186.39	50.16	358960.60	1.62	43.68	756.19	598.12	0.02	0.00081	0.36	0.15
PR192	192	wackestone																
PR194	194	mudstone-wackestone	6.23	-2.92														
PR196	196	wackestone																
PR198	198	wackestone	6.23	-2.69	-0.39	0.05	6163.82	130.19	42.54	360032.32	1.52	33.23	988.14	621.13	0.04	0.00054	0.30	0.13
PR200	200	wackestone																
PR201.6	201.6	wackestone	5.89	-2.95														
PR204	204	wackestone																
PR207	207	wackestone	5.85	-2.73	-0.48	0.06	3606.60	107.41	42.63	367180.14	1.36	29.67	455.81	678.37	0.02	0.00026	0.20	0.14
PR209	209	wackestone																
PR211	211	wackestone	5.62	-2.68														
PR213	213	mudstone-wackestone																
PR214	214	mudstone-wackestone	5.47	-2.80	-0.37	0.03	5261.34	113.53	38.75	369162.19	1.94	36.55	718.00	636.24	0.06	0.00066	0.25	0.23
PR215	215	mudstone-wackestone																

PR218	218	wackestone	5.07	-3.20														
PR221	221	wackestone	4.97	-3.55	-0.24	0.08	2819.70	169.46	41.50	357065.27	2.44	44.72	243.12	497.73	0.02	0.00010	0.34	0.22
PR223	223	mudstone-wackestone																
PR224	224	wackestone																
PR227	227	wackestone	4.71	-3.87	-0.38	0.02	3105.28	111.32	34.14	364260.47	1.72	26.84	77.35	577.17	0.01	0.00009	0.25	0.24
PR229	229	mudstone-wackestone																
PR231	231	mudstone-wackestone	4.36	-2.89	-0.26	0.08	4961.80	109.49	38.96	367060.64	1.94	30.80	96.20	539.82	0.02	0.00019	0.16	0.30
PR233	233	mudstone-wackestone																
PR235	235	mudstone-wackestone	3.51	-3.80														
PR237	237	wackestone																
PR239	239	wackestone	3.17	-3.41	-0.21	0.00	3477.66	177.58	39.75	365844.05	2.37	46.69	130.69	475.26	0.01	0.00015	0.26	0.36
PR241	241	mudstone																
PR244	244	mudstone-wackestone	3.00	-4.04	-0.33	0.03	3052.70	105.10	30.56	349251.89	2.66	48.84	199.34	493.84	0.02	0.00027	0.30	0.40
PR246	246	mudstone-wackestone																
PR248	248	mudstone-wackestone	2.55	-2.65	-0.51	0.00	3840.91	32.64	58.77	362154.75	3.36	76.82	77.93	326.93	0.04	0.00061	0.07	0.71
PR250	250	mudstone-wackestone																
PR252	252	mudstone-wackestone	1.97	-3.92														
PR19 shell		fossil			-0.38	0.08	1241.85	7.31	7.58	156921.24	0.57	4.74	9.05	138.46	0.03	0.00006	0.00	0.18
PRX23.5 crinoid		fossil			-0.57		3223.00	9.12	105.47	381614.03	1.46	71.61	17.02	317.45	0.01	0.00004	0.01	0.21
PR144 coral		fossil					1680.63	13.06	21.82	354776.49	0.12	10.88	7.95	312.04	0.01	0.00005	0.01	0.01
PR214 coral		fossil			-0.39	0.05	3591.95	9.70	18.35	348064.05	0.25	17.10	5.15	308.39	0.01	0.00007	0.00	0.03
PR80 (remeasured)	80	mudstone-wackestone			-1.02	0.15	3173.12	93.56	151.36	294544.76	6.36	67.84	345.04	680.75	0.01	0.00056	0.11	0.19